# Doping-Engineered Praseodymium–Barium Cobaltite Oxides for Dual Oxygen and Lithium Ionic Diffusivity in Offshore Metal–Air Batteries

Sasan Rezaee[1,2] **, Hossein Darban[3]*, Nilüfer Ertekin[4], Fatemeh Mohammad Dezashibi[1], Houshyar Noshad[1], and Ould el Moctar[2]

[1] Department of Physics and Energy Engineering, Amirkabir University of Technology, Tehran 159163-4311, Iran

[2] Institute of Sustainable and Autonomous Maritime Systems, University of Duisburg-Essen, Duisburg, 47057, Germany

[3] Institute of Fundamental Technological Research, Polish Academy of Sciences, Pawińskiego 5B, 02-106 Warsaw, Poland

[4] Department of Electrical and Electronics Engineering, Yalova University, Yalova, Turkey

**Corresponding Authors:**

* Hossein Darban (hdarban@ippt.pan.pl); ** Sasan Rezaee (sasan.rezaee@uni-due.de)

## Abstract

This research conducts comprehensive molecular dynamics simulations on doped double perovskites, $PrBa_{(1-x)}A'_xCo_{(2-y)}B'_yO_{5+\delta}$ ($0 \leq x \leq 0.25$, $0 \leq y \leq 0.25$, and $0.375 \leq \delta \leq 0.500$), as catalyst in metal–air batteries to systematically evaluate various doping strategies and identify the most effective approach for enhancing ionic diffusion. In addition, the application of metal–air batteries and their modifications for offshore power plants have been addressed. Four types of doping were studied: (i) substitution at $Ba^{2+}$ sites with $Sr^{2+}$, $Ca^{2+}$, or $Na^{+}$; (ii) substitution at $Co^{3+}$ sites with $Fe^{3+}$, $Cr^{3+}$, $Mn^{3+}$, $Ni^{3+}$, $Al^{3+}$, or $Zn^{2+}$; (iii) dual-site doping with $Na^{+}$ and $Zn^{2+}$ at $Ba^{2+}$ and $Co^{3+}$ sites, respectively; and (iv) interstitial doping with $Li^{+}$ ions. Among single-site dopants, $Na^{+}$ at the Ba-site and $Zn^{2+}$ at the Co-site, as well as dual-site–doped $PrBa_{0.875}Na_{0.125}Co_{1.875}Zn_{0.125}O_{5.375}$, exhibit better oxygen ion mobility. In contrast, interstitial $Li^{+}$ doping in $Li_{0.125}$-doped $PrBa_{0.9375}Co_2O_{5.5}$ provides better oxygen diffusivity, comparable to other samples, and additionally enables significant $Li^{+}$ mobility. $Li_{0.125}$-doped $PrBa_{0.9375}Co_2O_{5.5}$, with dual oxygen-lithium diffusivity roles, needs to be combined with doped porous carbon materials and metal oxides as a matrix, and transition metal oxide catalysts coated with bio-inspired oxygen-selective-membrane to guarantee operation in offshore environments with high humidity.

**Keywords:** Metal-air batteries, Double perovskite oxide, Doping, Diffusivity, Offshore power plants.

## 1. Introduction

Current state-of-the-art lithium-ion batteries have achieved remarkable advancements that were once unimaginable decades ago, such as enabling modern vehicles to operate on clean energy instead of fossil fuels. Nevertheless, the demand for energy storage devices with even greater performance continues to grow. Rechargeable Lithium-air batteries (LABs) are considered a promising alternative to current lithium-ion batteries (LIBs) and are expected to enter the market by 2030 [1,2]. With their high theoretical energy density, suitable operating voltage range, and low manufacturing cost, LABs have the potential to significantly advance modern technological development and contribute to achieving the net-zero target [3–5]. However, the main challenges of current LABs for industrialization are low cycling life, poor coulombic efficiency, capacity fading, slow charging rates, and cathode degradation [6]. Part of these challenges can be mitigated by utilizing a solid-electrolyte-interphase on the anode side; however, different strategies are required on the cathode side [7]. It has been demonstrated that most of the challenges hindering the further advancement of LABs are caused by the sluggish kinetics of the oxygen reduction reaction (ORR) in discharge and oxygen evolution (OER) reaction in charge processes at the cathode side [8,9]. Therefore, the main pathway, and also the primary challenge, toward building a LAB with high cyclability and capacity is the design of an appropriate cathode [10].

A satisfactory cathode in a LAB should demonstrate a sufficiently porous structure, electrochemical stability, high electrical conductivity, and an enlarged specific surface area [9]. The objective is to facilitate the transport of oxygen, electrons, and lithium ions while maintaining ease and cost-effectiveness in fabrication. These requirements have guided researchers to utilize carbon-based materials as cathodes in LABs [11–13]. A significant challenge to the practical realization of LABs is the penetration of air components, such as water vapor ($H_2O$), carbon dioxide ($CO_2$), and Nitrogen gas ($N_2$), into the cell. These components react with lithium, forming undesired byproducts, including lithium hydroxide (LiOH), lithium carbonate ($Li_2CO_3$), and trilithium nitride ($Li_3N$). These undesired byproducts are difficult to decompose, and their continuous formation and accumulation on the cathode surface hinder efficient ORR and OER reactions, thereby leading to inferior cell performance [14,15]. Recent advancements in the field have encompassed the development of carbon-based composite cathodes and the integration of diverse catalysts [16–18].

The utilization of catalysts at the cathode of LABs enhances the ORR and OER reactions, influencing the properties of the desired reversible discharge product, lithium peroxide ($Li_2O_2$) [19]. In addition, catalysts significantly improve the performance of LABs by increasing cyclability and reducing the formation of undesirable byproducts (LiOH, $Li_2CO_3$, $Li_3N$). So far, six different types of cathode catalysts have been used in LABs: precious metals and/or their oxides, transition metals and/or their

oxides, carbides, sulfides, nitrides, and perovskite oxides [2,9]. These catalysts are expected to effectively facilitate both ORR and OER reactions and operate across a wide range of temperatures, resulting from, for example, seasonal variations or external thermal sources. Additionally, their performance can be further enhanced by microporosity, which promotes oxygen diffusion within the cathode [20]. Consequently, the ability to facilitate both ORR and OER reactions, proper thermal stability, suitable chemical resistance, and a microporous structure are essential characteristics of an efficient cathode catalyst for LABs. All of these characteristics are provided by catalysts based on perovskite materials [20,21].

Single perovskite oxides have the general formula $ABO_3$, in which A and B are large electropositive cations and O is oxygen anion. Research on single perovskite oxides as oxygen electrocatalysts began in the early 1970s with the work reported in [22]. It was shown that $LaCoO_3$ is a promising material; improvements in conductivity were observed through Sr or Ni doping. Later, various transition metal-based perovskites (e.g., $LaMnO_3$, $SrFeO_3$) were evaluated for ORR and OER reactions [23,24]. For instance, perovskites with larger A-site cations (e.g., $La^{3+}$) favored symmetric structures and exhibited better electrocatalytic performance [25]. Double perovskites, which are formed by expanding single perovskite structures, have the general formula $AÁBB́O_6$. They have notable advantages over conventional single perovskites, including enhanced oxygen ion diffusion, more rapid surface oxygen exchange, and improved electrical conductivity [26–28]. The enhanced electron and ion conductivity of double perovskites can be further improved through doping [29] and nanoscale miniaturization [30].

Studies have shown that double perovskites of the form $LnBaCo_2O_{5.5}$ (Ln=Pr, Nd, Gd) are excellent candidates for use as catalysts in metal–air batteries due to their high inherent concentration of oxygen vacancies, enhanced oxygen ion diffusion, and improved ORR and OER activities [27,29–38]. One characteristic feature of this family of double perovskites is the presence of 0.5 oxygen vacancy per formula unit, which contributes to enhanced oxygen ion transport and catalytic activity. The double perovskite $PrBaCo_2O_{5+\delta}$ was first synthesized and characterized in the late 1990s [39]. In this structure, $\delta$ is a dimensionless number between 0 and 1, where $1-\delta$ represents the number of oxygen vacancies per formula unit. Later, it has been shown that the most probable structural phases of this double perovskite are orthorhombic and tetragonal phases [40].

The high concentration of oxygen vacancies in the double perovskite $PrBaCo_2O_{5+\delta}$ has motivated several pioneering studies on this structure. Static atomistic simulations based on the Born model, conducted on double perovskites of the form $LnBaCo_2O_{5.5}$ (Ln = Y, La, Pr, Nd, Sm, Gd, Dy, Ho, Er, and Yb), showed that $PrBaCo_2O_{5.5}$ provides the most efficient balance between two competing effects: a low oxygen Frenkel energy (as low as 0.24 eV per defect) and a high antisite energy (up to 0.94 eV) [41].

Further molecular dynamics (MD) simulations on $PrBaCo_2O_{5.5}$ [42] revealed an anisotropic oxygen diffusion mechanism, occurring predominantly in the Pr-O and Co-O planes, with an activation energy of 0.35 eV. Doping has been demonstrated to be an effective method for enhancing the catalytic properties of $PrBaCo_2O_{5+\delta}$ [30] and improving oxygen diffusivity, ionic and electronic conductivity, and finally catalytic activities. The literature review reveals that doping alkaline earth metals (Sr and Ca) into the barium (Ba) sublattice and transition metals (Fe, Cu, Ni, and Al) into the cobalt (Co) site in $PrBaCo_2O_{5+}\delta$ alters the oxygen diffusion coefficient and electrical conductivity [30,34–36,38,43–45]. However, due to variations in dopant ion concentrations, temperature, and pressure in the reported data, it is challenging to determine which host ions and doping strategies yield the maximum efficiency.

Despite its significance, a comprehensive study on the $PrBaCo_2O_{5+\delta}$ that systematically investigates the effects of doping with various elements at Ba- and/or Co-sites under equivalent conditions is still lacking in the literature. This scientific gap becomes even more critical given that the $PrBaCo_2O_{5+\delta}$ is a promising catalyst candidate for various metal–air batteries, including aluminum–air (Al–air), lithium–air (Li–air), zinc–air (Zn–air), and sodium–air (Na–air) systems [46,47]. However, it remains unknown for which of these batteries this catalyst demonstrates the highest efficiency. Therefore, this study employs MD simulations to investigate the oxygen diffusivity in the $PrBaCo_2O_{5+\delta}$ doped with Fe, Cr, Mn, Ni, Al, Zn, Sr, Ca, Na, and Li ions. Additionally, this study investigates how doping with these ions affects the anisotropic oxygen diffusion mechanism. The impact of doping at the Ba and Co sites, both individually and concurrently, is systematically examined. In other words, the current work investigates oxygen diffusivity properties in $PrBa_{(1-x)}A'_xCo_{(2-y)}B'_yO_{5+\delta}$, where A'=Sr, Ca, and Na, and B'=Fe, Cr, Mn, Ni, Al, and Zn for $0 \leq x \leq 0.25$ and $0 \leq y \leq 0.25$. The Li is doped in interstitial sites.

## 2. Molecular Dynamics Simulations

### 2.1. Initial Atomic Configuration of $PrBaCo_2O_{5.5}$

In general, $PrBaCo_2O_{5.5}$ has two orthorhombic and one tetragonal structural phase [48,49]. The orthorhombic phases with space groups *Pmma* and *Pmmm* are stable at 300-344 and 344-776 K, respectively, while the tetragonal phase with *P*4/*mmm* space group is stable at 776-1600 K [48,49]. This high-temperature tetragonal phase is adopted for the MD simulations conducted in this study. To generate the initial atomic configuration of $PrBaCo_2O_{5.5}$, the unit cell of this double perovskite in the *P*4/*mmm* phase is first defined based on the previous studies [31,33–36,42,48–50]. The tetragonal structure of $PrBaCo_2O_6$ consists of 10 atomic basis sites [31]: one site for $Pr^{3+}$, one for $Ba^{2+}$, two for $Co^{3+}$, and six for $O^{2-}$. Fig. 1(a) illustrates the primitive cell of $PrBaCo_2O_6$. Repeating this unit cell twice creates a supercell of $2PrBaCo_2O_6$ with a total electrostatic charge of $-2|e|$. Removing one oxygen ion from this supercell

neutralizes the charge, resulting in a charge-balanced $PrBaCo_2O_{5.5}$ and showing 0.5 inherent oxygen vacancies per cell. To construct the Bravais lattice using a similar strategy, the $PrBaCo_2O_6$ unit cell is further replicated along the crystallographic directions x [100], y [010], and z [001] by factors of 8, 8, and 4, respectively (see Fig. 1(b)) to create 256 supercells. Subsequently, 128 oxygen ions were randomly deleted from the Bravais lattice to neutralize the electrostatic charge. This results in a Bravais lattice containing 256 $Pr^{3+}$, 256 $Ba^{2+}$, 512 $Co^{3+}$, 1408 $O^{2-}$ ions, and 128 oxygen vacancies ($\ddot{V}_O$).

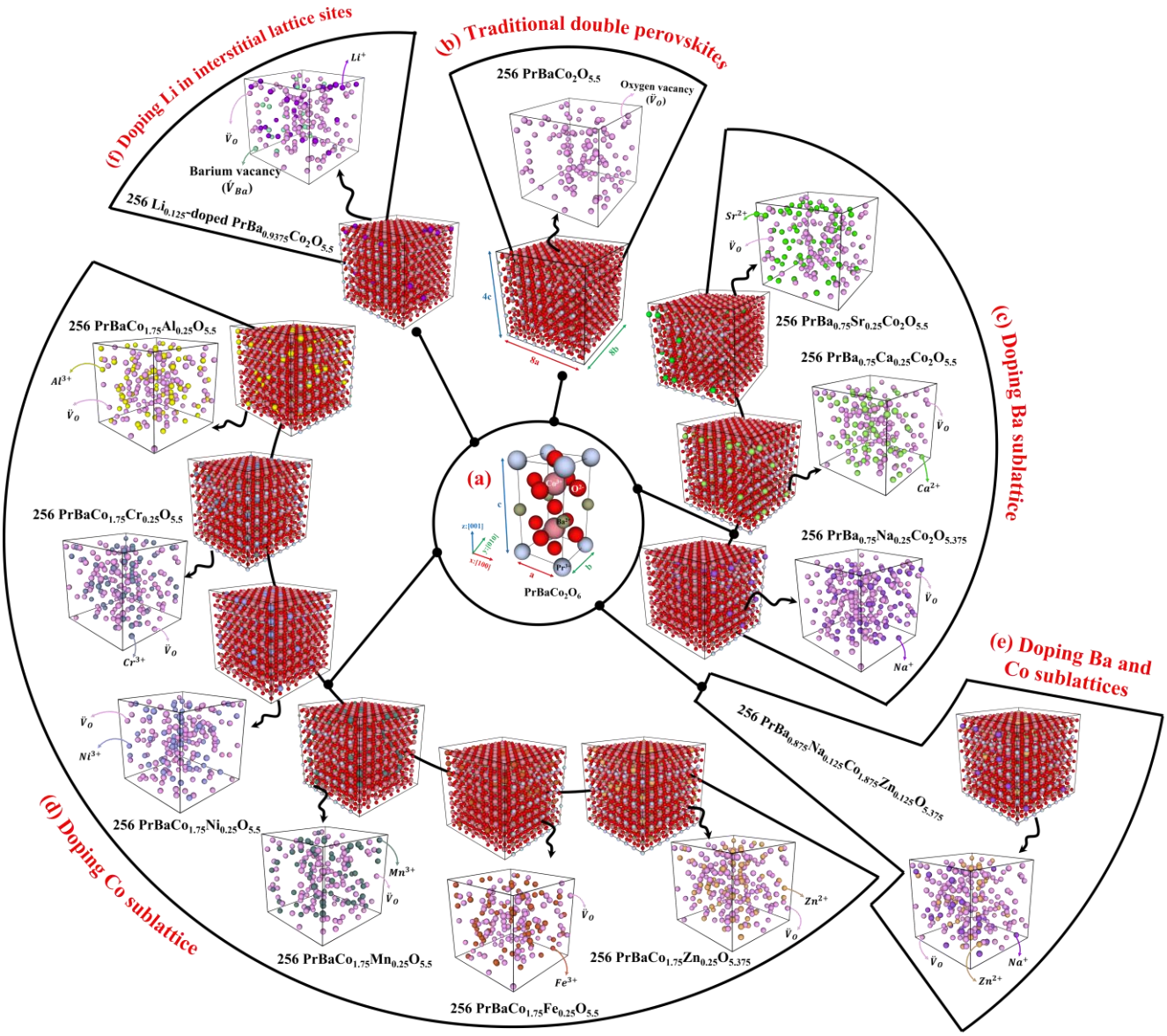


**Fig. 1** (a) $PrBaCo_2O_6$ unit cell, (b) the initial atomic configuration of 256 $PrBaCo_2O_{5+5}$, (c) 256 $PrBa_{(1-x)}A'_xCo_2O_{5+\delta}$, (d) 256 $PrBaCo_{(2-y)}B'_yO_{5+\delta}$, (e) 256 $PrBa_{0.875}Na_{0.125}Co_{1.875}Zn_{0.125}O_{5.375}$, and (f) 256 $Li_{0.125}$-doped $PrBa_{0.9375}Co_2O_{5.5}$. Here, A'=Sr, Ca, and Na, and B'=Fe, Cr, Mn, Ni, Al, and Zn for x=y = 0.25, and $0.375 \leq \delta \leq 0.500$

## 2.2. Initial Atomic Configuration of $PrBa_{(1-x)}A'_xCo_{(2-y)}B'_yO_{5+\delta}$

To generate the initial atomic configuration of double perovskite $PrBa_{(1-x)}A'_xCo_{(2-y)}B'_yO_{5+\delta}$, where A'=Sr, Ca, and Na, and B'=Fe, Cr, Mn, Ni, Al, and Zn for $0 \leq x \leq 0.25$, $0 \leq y \leq 0.25$, and $0.375 \leq \delta \leq 0.500$, the similar approach like pervious section is used to generate $\ddot{V}_O$. Moreover, to dope an ion at either the Ba or Co sites, the corresponding site is selected randomly for the replacement. Fig. 1 depicts all of the investigated configurations in the current study. The foreign (guest) ions were selected based on their matching electronegativity and ionic radius relative to the intrinsic (host) ions in the corresponding sublattice. In other words, dopant ions in the $Ba^{2+}$ sublattice need to exhibit similar electronegativity and ionic radius to $Ba^{2+}$ to prevent dislocations and crystal instability. A similar condition needs to be considered for the $Co^{3+}$ sublattice. Table S1 compares the ionic radii and electronegativities of the ions involved in the simulations. Based on the data in this table, doping with the guest ions does not disrupt the overall charge balance, except in three cases: when $Na^+$ is doped at $Ba^{2+}$ sites, when $Zn^{2+}$ is doped at $Co^{3+}$ sites, and $Li^+$ is doped in interstitial sites. For $Na^+$ and $Zn^{2+}$ cases, charge neutrality is restored by introducing an appropriate number of oxygen vacancies. For $Li^+$, creating barium vacancies restores the electrostatic charge balance.

The foreign ions are chosen for doping due to five strategic reasons. First, elements like Al, Li, Zn, and Na have vast applications in Al-air, Li-air, Zn-air, and Na-air batteries. Second, Fe, Cr, Mn, Ni, and Zn are transition metals whose doping in oxide catalysts can generally enhance OER activity by modulating the covalent bonding between the transition metal and oxygen. Third, Sr and Ca, belonging to the alkaline-earth metals group, are considered to enable doping at the Ba site. Additionally, these two elements have shown positive effects in improving catalytic properties in previous studies [30,38]. Fourth, Na alkali metal due to its monovalent nature (+1 valence), can effectively promote the formation of oxygen vacancies, which enhances oxygen ion diffusion and the catalytic activity for ORR. Fifth, due to its small ionic radius, the alkali metal $Li^+$ tends to occupy interstitial lattice sites [51], which can contribute to Li diffusivity in addition to oxygen diffusion, thereby increasing the probability of discharge product formation.

Inspired by previous empirical studies [30,44], the doping concentrations in $PrBa_{(1-x)}A'_xCo_{(2-y)}B'_yO_{5+\delta}$ are limited to the range of 0 to 0.25. Furthermore, to enable a direct comparison of the effects of doping at the $Ba^{2+}$ and $Co^{3+}$ sites, the doping concentrations are defined using the following equations:

$$x = \frac{Number\ of\ doped\ foreign\ cations\ (Sr^{2+}\ or\ Ca^{2+}\ or\ Na^{1+})}{Number\ of\ Ba^{2+}\ in\ perfect\ crystal} \quad (1)$$

$$y = 2 \times \left(\frac{Number\ of\ doped\ foreign\ cations\ (Fe^{3+}\ or\ Cr^{3+}\ or\ Mn^{3+}\ or\ Ni^{3+}\ or\ Al^{3+}\ or\ Zn^{2+})}{Number\ of\ Co^{3+}\ in\ perfect\ crystal}\right) \quad (2)$$

Here, x and y represent the doping concentrations at the $Ba^{2+}$ and $Co^{3+}$ sublattices, respectively. The coefficient of 2 in Eq. (2), arises from the stoichiometry of $Co^{3+}$ in the chemical formula $PrBaCo_2O_6$, where two $Co^{3+}$ are present per formula unit. For instance, for modeling 256 $PrBa_{(1-x)}A'_xCo_{(2-y)}B'_yO_{5+\delta}$ with $x = y = 0.25$, a total of 64 A' and 64 B' ions must be doped into the structure. As mentioned earlier, in the cases of doping with $Na^+$ and $Zn^{+2}$, additional oxygen vacancies must be introduced to maintain charge neutrality. The number of required $\ddot{V}_O$ is determined based on the following formula:

$$\delta' = 6 \times \left(\frac{Number\ of\ intrinsic\ \ddot{V}_O + Number\ of\ \ddot{V}_O\ induced\ by\ doping}{Number\ of\ O^{2-}\ in\ perfect\ crystal\ (256PrBaCo_2O_6)}\right) \quad (3)$$

$$\delta = 1 - \delta' \quad (4)$$

where $\delta'$ is the concentration of the oxygen vacancies. In addition, the "number of intrinsic $\ddot{V}_O$" corresponds to the oxygen vacancies present in the simulated 256 $PrBaCo_2O_{5.5}$ structure described in the previous section is equal to 128. The "number of $\ddot{V}_O$ induced by doping" refers to the additional oxygen vacancies introduced into the structure as a result of $Na^+$ and $Zn^{+2}$ doping. The coefficient of 6 in the definition of $\delta'$ arises from the stoichiometry of $O^{2-}$ in the chemical formula $PrBaCo_2O_6$, where six oxygen ions are present per formula unit. In general, to maintain charge neutrality, one oxygen ion must be removed from the structure for every two $Na^+$ and $Zn^{+2}$ ions introduced through doping in $Ba^{2+}$ and $Co^{3+}$ sublattice, respectively. In the previous example, where $x = y = 0.25$, a total of 32 oxygen ions are removed from the structure upon doping with 64 $Na^+$ or $Zn^{+2}$ ions in $Ba^{2+}$ and $Co^{3+}$ sublattices, respectively. In Eq. (3), the number of $O^{2-}$ ions in perfect crystal 256 $PrBaCo_2O_6$ is equal to 1536. Therefore, for the case with $x = y = 0.25$, the concentration of oxygen vacancy is determined as $\delta' = 0.625$.

Upon $Li^+$ doping in interstitial lattice sites, the net charge of the system becomes positive, which necessitates a reduction in the overall positive charge. An appropriate approach is to reduce the number of $Ba^{2+}$ ions in the structure, as it has been shown that removing $Ba^{2+}$ ions alters the electrostatic charge distribution of the structure less than removing $Co^{3+}$ or $Pr^{3+}$ ions [7,44]. In general, one $Ba^{2+}$ ion should be removed from the structure for every two $Li^+$ ions doped, to maintain charge neutrality. The concentration of barium vacancies ($\xi$) can be calculated from the following equation:

$$\xi = \frac{(Number\ of\ doped\ Li^{+}/2)}{Number\ of\ Ba^{2+}\ in\ perfect\ crystal\ (PrBaCo_2O_{5\cdot5})} \quad (5)$$

To study oxygen diffusivity in 256 $Li_{0.2\xi}$-doped $PrBa_{(1-\xi)}Co_2O_{5.5}$, 32 $Li^+$ ions are randomly placed in interstitial lattice sites, while 16 $Ba^{2+}$ ions are randomly removed. Using Eq. (5), the concentration of barium vacancies is calculated as $\xi = 0.0625$. Therefore, 256 $Li_{0.2\xi}$ -doped $PrBa_{(1-\xi)}Co_2O_{5.5}$ has 32 $Li^+$, 256 $Pr^{3+}$, 240 $Ba^{2+}$, 512 $Co^{3+}$, 1408 $O^{2-}$ ions, as well as 128 $\ddot{V}_O$, and 16 barium vacancies ( $\acute{V}_{Ba}$). The formula units of the studied doped double perovskites are listed in Table 1. The initial atomic configurations are shown in Fig. 1.

**Table 1:** The formula units of the studied double perovskites.

| **256 $PrBaCo_2O_{5.5}$** | | | | | | | | | | | | | | |
|---|---|---|---|---|---|---|---|---|---|---|---|---|---|---|
| Sample | x | y | ξ | δ | $Pr^{3+}$ | $Ba^{2+}$ | $N\acute{V}_{Ba}$ | A' | NA' | $Cr^{3+}$ | B' | NB' | $O^{2-}$ | $N\ddot{V}_O$ |
| 256$PrBaCo_2O_{5.5}$ | 0 | 0 | 0.0000 | 0.500 | 256 | 256 | 0 | 0 | 0 | 512 | 0 | 0 | 1408 | 128 |
| **256 $PrBa_{(1-x)}A'_xCo_2O_{5+\delta}$** | | | | | | | | | | | | | | |
| Sample | x | y | ξ | δ | $Pr^{3+}$ | $Ba^{2+}$ | $N\acute{V}_{Ba}$ | A' | NA' | $Cr^{3+}$ | B' | NB' | $O^{2-}$ | $N\ddot{V}_O$ |
| 256 $PrBa_{0.75}Sr_{0.25}Co_2O_{5.5}$ | 0.25 | 0 | 0.0000 | 0.500 | 256 | 192 | 0 | $Sr^{2+}$ | 64 | 512 | 0 | 0 | 1408 | 128 |
| 256 $PrBa_{0.75}Ca_{0.25}Co_2O_{5.5}$ | 0.25 | 0 | 0.0000 | 0.500 | 256 | 192 | 0 | $Ca^{2+}$ | 64 | 512 | 0 | 0 | 1408 | 128 |
| 256 $PrBa_{0.75}Na_{0.25}Co_2O_{5.375}$ | 0.25 | 0 | 0.0000 | 0.375 | 256 | 192 | 0 | $Na^+$ | 64 | 512 | 0 | 0 | 1376 | 160 |
| **256 $PrBaCo_{(2-y)}B'_yO_{5+\delta}$** | | | | | | | | | | | | | | |
| Sample | x | y | ξ | δ | $Pr^{3+}$ | $Ba^{2+}$ | $N\acute{V}_{Ba}$ | A' | NA' | $Cr^{3+}$ | B' | NB' | $O^{2-}$ | $N\ddot{V}_O$ |
| 256 $PrBaCo_{1.75}Fe_{0.25}O_{5.5}$ | 0 | 0.25 | 0.0000 | 0.500 | 256 | 256 | 0 | 0 | 0 | 448 | $Fe^{3+}$ | 64 | 1408 | 128 |
| 256 $PrBaCo_{1.75}Cr_{0.25}O_{5.5}$ | 0 | 0.25 | 0.0000 | 0.500 | 256 | 256 | 0 | 0 | 0 | 448 | $Cr^{3+}$ | 64 | 1408 | 128 |
| 256 $PrBaCo_{1.75}Mn_{0.25}O_{5.5}$ | 0 | 0.25 | 0.0000 | 0.500 | 256 | 256 | 0 | 0 | 0 | 448 | $Mn^{3+}$ | 64 | 1408 | 128 |
| 256 $PrBaCo_{1.75}Ni_{0.25}O_{5.5}$ | 0 | 0.25 | 0.0000 | 0.500 | 256 | 256 | 0 | 0 | 0 | 448 | $Ni^{3+}$ | 64 | 1408 | 128 |
| 256 $PrBaCo_{1.75}Al_{0.25}O_{5.5}$ | 0 | 0.25 | 0.0000 | 0.500 | 256 | 256 | 0 | 0 | 0 | 448 | $Al^{3+}$ | 64 | 1408 | 128 |
| 256 $PrBaCo_{1.75}Zn_{0.25}O_{5.375}$ | 0 | 0.25 | 0.0000 | 0.375 | 256 | 256 | 0 | 0 | 0 | 448 | $Zn^{2+}$ | 64 | 1376 | 160 |
| **256 $PrBa_{(1-x)}A'_xCo_{(2-y)}B'_yO_{5+\delta}$** | | | | | | | | | | | | | | |
| Sample | x | y | ξ | δ | $Pr^{3+}$ | $Ba^{2+}$ | $N\acute{V}_{Ba}$ | A' | NA' | $Cr^{3+}$ | B' | NB' | $O^{2-}$ | $N\ddot{V}_O$ |
| 256 $PrBa_{0.875}Na_{0.125}Co_{1.875}Zn_{0.125}O_{5.375}$ | 0.125 | 0.125 | 0.0000 | 0.375 | 256 | 224 | 0 | $Na^+$ | 32 | 480 | $Zn^{2+}$ | 32 | 1376 | 160 |
| **256 $Li_{0.2\xi}$-doped $PrBa_{(1-\xi)}Co_2O_{5+\delta}$** | | | | | | | | | | | | | | |
| Sample | x | y | ξ | δ | $Pr^{3+}$ | $Ba^{2+}$ | $N\acute{V}_{Ba}$ | A' | NA' | $Cr^{3+}$ | B' | NB' | $O^{2-}$ | $N\ddot{V}_O$ |
| 256 $Li_{0.125}$-Doped $PrBa_{0.9375}Co_2O_{5.5}$ | 0 | 0 | 0.0625 | 0.500 | 256 | 240 | 16 | 0 | 0 | 512 | 0 | 0 | 1408 | 128 |

x: Doping concentration at the $Ba^{2+}$ site
y: Doping concentration at the $Co^{3+}$ site
ξ: Concentration of barium vacancies due to lithium-doping
δ: Deviation from the ideal oxygen content
$N\acute{V}_{Ba}$: Number of barium vacancies
A': Guest element at the $Ba^{2+}$ site
NA': Number of guest elements at the $Ba^{2+}$ site
B': Guest element at the $Co^{3+}$ site
NB': Number of guest elements at the $Co^{3+}$ site
$N\ddot{V}_O$: Number of oxygen vacancies
2ξ: Number of doped $Li^+$ ions in interstitial lattice sites

## 2.3. Simulation Details

The classical MD is used in this work to study the oxygen diffusivity in the double perovskites described in Sections 2.1 and 2.2. The MD simulations are conducted using the Large Scale Atomic/Molecular Massively Parallel Simulator (LAMMPS) [52] and the obtained results are visualized and analyzed using

the Visual Molecular Dynamics (VMD) software [53] and the Open Visualization Tool (OVITO) [54]. Periodic boundary conditions are imposed in all three dimensions to model the oxygen diffusivity in the bulk of double perovskites. A time step of 1 femtosecond (fs) and Verlet-style neighbor list methodology are utilized throughout the simulations. Atomic velocities at the studied temperatures are defined using the Maxwell-Boltzmann distribution. The velocity form of the Stoermer-Verlet time integration algorithm (velocity-Verlet) is used [55]. Energy minimization at 0 K was performed using the conjugate gradient (CG) method with the Polak–Ribiere (PR) variant, as implemented in LAMMPS.

After energy minimization, a two-step equilibration process is performed on the double perovskites [34,35]. In the first step, the system is equilibrated for 500 picoseconds (ps) at the target temperature and a pressure of 0 Pa using the NPT ensemble. Temperature and pressure are controlled using a Nose–Hoover thermostat and barostat, respectively. In the second step, the system is further equilibrated for another 500 ps using the NVT ensemble. After this two-step equilibration process, the thermodynamic characteristics and lattice parameters reach equilibrium. After equilibration, the simulation continued for 1 nanosecond (ns) under the NVT ensemble at the corresponding temperature to measure the mean square displacement (MSD), diffusion coefficient, and activation energy. Additionally, the inter-ionic distances in the system were analyzed using the radial distribution function (RDF). The simulations were performed separately at five different temperatures: 873, 923, 973, 1273, and 1323 K.

The MSD and RDF were obtained directly from LAMMPS outputs. The diffusion coefficients were calculated from the slope of the MSD versus time curves (see Fig. S2). In the two-dimensional *a*–*b* plane (see Fig. 1), the diffusion coefficient is given by dividing the slope by four, while along the *c*-axis it is obtained by dividing the slope by two. The diffusion activation energy was determined by analyzing the temperature dependence of the diffusion coefficients. Specifically, a linear fit was applied to the plot of the natural logarithm of the diffusion coefficient versus the inverse of the absolute temperature (see Fig. S3). This Arrhenius plot yields a slope that is directly proportional to the activation energy. More information regarding RDF, MSD, activation energy, as well as the formal analysis methods, has been comprehensively described in authors' previous works [7,56].

### 2.4. Interatomic Potential

Following Refs. [31,50,57–60], the interatomic interactions are modeled using the combination of the standard long-range Coulombic potential ($U_{Coulombic}^{Long\ range}$) and the short-range Buckingham potential ($U_{Buckingham}^{Short\ range}$):

$$U_r(r) = U_{Coulombic}^{Long\ range}(r) + U_{Buckingham}^{Short\ range}(r) = \left(\frac{q_i q_j}{r}\right) + \left(Ae^{-\frac{r}{\rho}} - \frac{C}{r^6}\right) \quad , \quad r \le r_c \tag{6}$$

where $q_i$ and $q_j$ are the electrostatic charges of the pair of ions $i$ and $j$, and $r$ is their distance. The parameters $A$, $\rho$, and $C$ are the coefficients of the Buckingham potential. The cutoff distance, $r_c$, is 11 Å [31,42]. For radii exceeding the cutoff radius, long-range Coulombic interactions were calculated using the Ewald summation method with an accuracy of $10^{-6}$ [31]. The coefficients of the potential defined in Eq. (6) are listed in Table S.2. These coefficients, taken from existing literature, were obtained using semi-empirical approaches based on the density functional theory (DFT) and experimental data [31,50,57–60] and can successfully describe and predict the physical properties of $PrBaCo_2O_{5.5}$ double perovskite and their doped configurations.

## 3. Results and Discussions

In the remainder of this section, first, verification criteria have been provided for the simulation algorithm and potential functions. To achieve this aim, the MD simulation setup described in Section 2 is verified by comparing the results for the crystal phase, lattice constants, diffusion coefficient, and activation energy of $PrBaCo_2O_{5.5}$ with available data from the literature. Then, the anisotropic oxygen diffusion in double perovskites $PrBa_{(1-x)}A'_xCo_{(2-y)}B'_yO_{5+\delta}$ is studied. First, the effect of doping various ions at the $Ba^{2+}$ sites is investigated. Then, a similar analysis is conducted to assess the effect of doping at the $Co^{3+}$ sites. Based on the results of these two analyses, the third step examines the effect of simultaneous doping at both $Ba^{2+}$ and $Co^{3+}$ sites. Finally, the $Li_{0.125}$-doped $PrBa_{0.9375}Co_2O_{5.5}$ structure is analyzed.

### 3.1. Verification

Figure S1 compares the RDF diagrams of $PrBaCo_2O_{5.5}$ at two temperatures, 873 K and 1323 K. At both temperatures, the RDFs exhibit sharp and regular peaks up to a distance of 11 Å. This indicates the persistence of long-range order and confirms that the structure remains in a stable solid phase as the temperature increases. The lattice parameters extracted from the RDF analysis are listed in Table S3 for five different temperatures. The obtained values are in excellent agreement with previously reported experimental and numerical data in the literature [34,48,61,62]. The temporal variation of MSD in the *a*-*b* plane and along the *c*-axis is illustrated in Fig. S2 for $PrBaCo_2O_{5.5}$ at 873 K. The plots of the natural logarithm of the determined diffusion coefficient versus 1000/T (K) are shown in Fig. S3 for diffusion in the *a*–*b* plane and along the *c*-axis at five different temperatures. The data shown in this figure are used to calculate the diffusion activation energy, which is determined to be 0.4079 eV for diffusion in

the *a–b* plane and 0.3491 eV along the *c*-axis, respectively. All the above-mentioned data are in good agreement with the reported data in the literature for $PrBaCo_2O_{5.5}$ [34,35,42].

### 3.2. Oxygen diffusivity in $PrBa_{(1-x)}A'_xCo_2O_{5+\delta}$: x=0.25 and Ba-Site Doping

Results for the double perovskite $PrBa_{(1-x)}A'_xCo_2O_{5+\delta}$, with x = 0.25 and A′ = Sr, Ca, or Na as dopant ions at the $Ba^{2+}$ sites, are presented in this section. Accordingly, three doped structures are studied: 256 supercells of $PrBa_{0.75}Sr_{0.25}Co_2O_{5.5}$, $PrBa_{0.75}Ca_{0.25}Co_2O_{5.5}$, and $PrBa_{0.75}Na_{0.25}Co_2O_{5.375}$. The RDF diagrams of $PrBa_{0.75}Sr_{0.25}Co_2O_{5.5}$ and the other two doped double perovskites at 873 K and 1323 K are compared in Fig. 2(a) and Fig. S4, respectively. All diagrams exhibit sharp and regular peaks, indicating a stable solid phase across this temperature range with no signs of crystallographic dislocations. Therefore, doping with $Sr^{2+}$, $Ca^{2+}$, and $Na^{+}$ does not compromise thermal or structural stability.

The temporal variation of the internal pressure in $PrBa_{0.75}Sr_{0.25}Co_2O_{5.5}$, $PrBa_{0.75}Ca_{0.25}Co_2O_{5.5}$, and $PrBa_{0.75}Na_{0.25}Co_2O_{5.375}$ at 1323 K is compared with that of $PrBaCo_2O_{5.5}$ in Fig. S5. This high temperature serves as a critical condition for assessing the effect of doping on the internal pressure of the system. The figure shows that the internal pressure of the doped structures oscillates within the range of −0.99 to +0.99 GPa, with a mean value of approximately 0 Pa. The comparison leads to the conclusion that doping with $Sr^{2+}$, $Ca^{2+}$, and $Na^{+}$ ions does not significantly increase the internal pressure and, therefore, does not promote the formation of crystallographic dislocations. One contributing factor is that these dopant ions have ionic radii and electronegativities similar to those of the host $Ba^{2+}$ ion.

The temporal variations of the MSD for all ion types in $PrBa_{0.75}Sr_{0.25}Co_2O_{5.5}$ at 1273 K are presented in Fig. 2(b) for both diffusion in the *a–b* plane and along the *c*-axis. As evident from the figure, the MSD values for diffusion in the *a–b* plane are higher than those along the *c*-axis for all ions. Moreover, the figure indicates that only oxygen ions exhibit diffusive behavior, as their MSD curves increase linearly with time, whereas the MSDs of other ions remain nearly constant over time. The minor oscillations in MSDs of other ions are due to thermal fluctuations. A similar trend is observed for $PrBa_{0.75}Sr_{0.25}Co_2O_{5.5}$ at other temperatures. Additionally, the MSD curves for all ions in $PrBa_{0.75}Ca_{0.25}Co_2O_{5.5}$ and $PrBa_{0.75}Na_{0.25}Co_2O_{5.375}$ at the studied temperatures show similar behavior. The only difference is in the slope of the oxygen ion MSD curve, which is distinct for each composition and temperature (results are only shown for oxygen ions in the following).

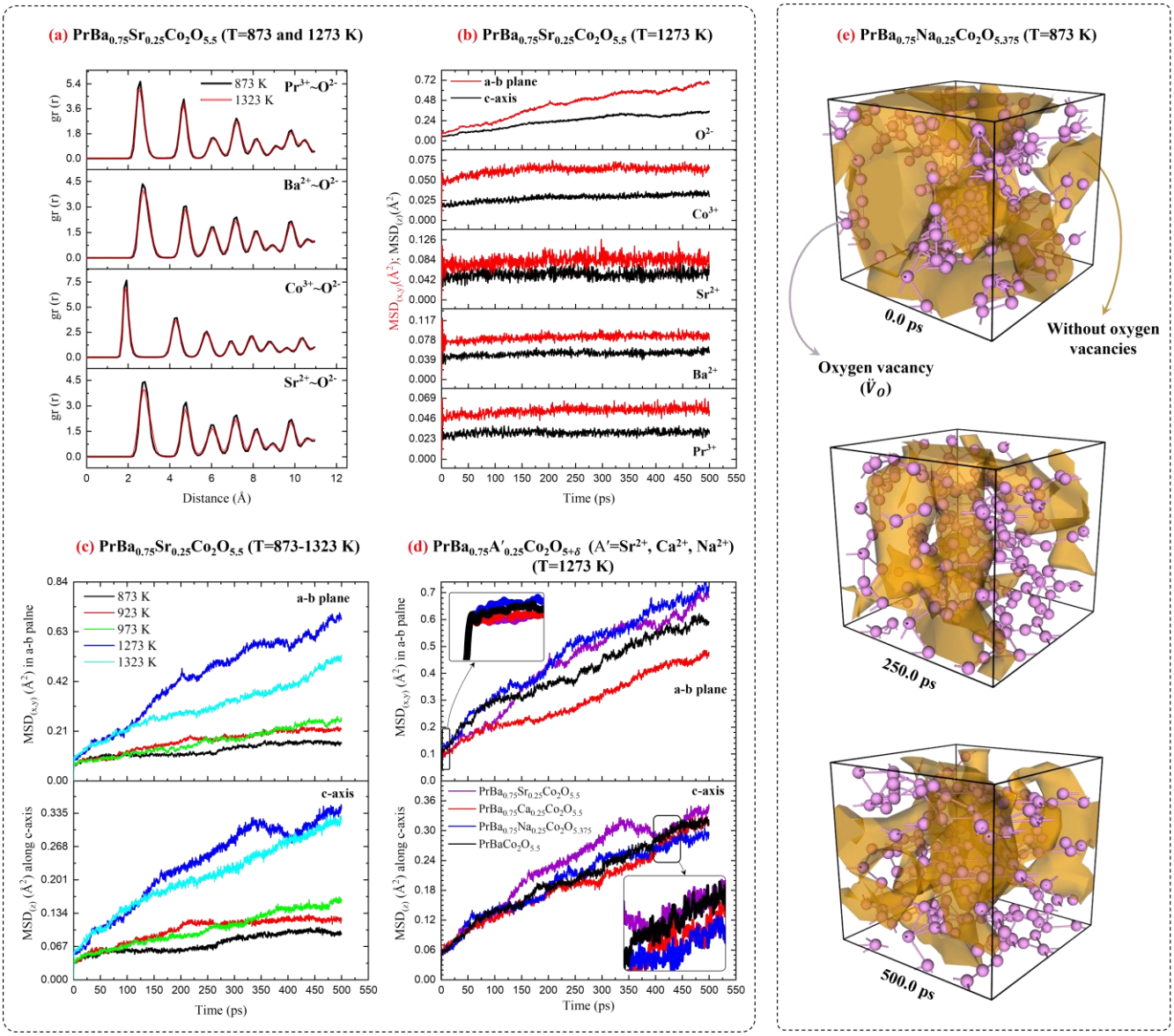


**Fig. 2** (a) The temporal variations of MSD related to all ions in $PrBa_{0.75}Sr_{0.25}Co_2O_{5.5}$ at 1273 K. (b) The temporal variations of MSD related to the oxygen ion in $PrBa_{0.75}Sr_{0.25}Co_2O_{5.5}$ at different temperatures. (c) The temporal variations of MSD related to the oxygen ion in $PrBa_{0.75}Sr_{0.25}Co_2O_{5.5}$, $PrBa_{0.75}Ca_{0.25}Co_2O_{5.5}$, $PrBa_{0.75}Na_{0.25}Co_2O_{5.375}$, and $PrBaCo_2O_{5.5}$, at 1273 K. (e) The snapshots of the $PrBa_{0.75}Na_{0.25}Co_2O_{5.375}$ configurations at 0.0, 250, and 500 ps include both oxygen vacancies (pink spheres) and regions without oxygen vacancies (orange mesh) at 873 K. Results are presented for ion diffusion in the *a*–*b* plane and along the *c*-axis.

The temporal variation of the MSD of oxygen ions at five different temperatures, ranging from 873 to 1323 K, is shown in Fig. 2(c) for $PrBa_{0.75}Sr_{0.25}Co_2O_{5.5}$. The results are presented separately for oxygen diffusion in the *a*–*b* plane and along the *c*-axis. Increasing the temperature from 873 to 1273 K generally increases the slope of the MSD curves, indicating a higher oxygen diffusion coefficient. However, a further increase to 1323 K does not enhance oxygen diffusivity along the *c*-axis and results in a decrease

in diffusivity in the *a–b* plane. The temporal variation of the MSD of oxygen ions in the other two double perovskites, $PrBa_{0.75}Ca_{0.25}Co_2O_{5.5}$ and $PrBa_{0.75}Na_{0.25}Co_2O_{5.375}$, showed similar trends but with different dependencies on temperature (results are only shown at 1273 K in the following).

The temporal variations of the MSD of oxygen ions at 1273 K for the original and all three doped $Ba^{2+}$ sites of double perovskites are shown in Fig. 2(d). The figure indicates that doping has minimal impact on oxygen diffusion along the *c*-axis; however, doping does influence oxygen diffusion in the *a–b* plane. Doping with $Ca^{2+}$ ions reduces the oxygen diffusivity in the *a–b* plane, whereas doping with either $Sr^{2+}$ or $Na^{+}$ ions increases the oxygen diffusion coefficient in the *a–b* plane. Doping with $Na^{+}$ ions enhances oxygen diffusivity more than $Sr^{2+}$ ions, mostly due to the increased oxygen vacancy concentration resulting from the reduced oxygen content in the Na-doped structure.

Fig. 2(e) illustrates three snapshots of the $PrBa_{0.75}Na_{0.25}Co_2O_{5.375}$ at 0.0, 250.0, and 500.0 ps, revealing two main regions: those with and without oxygen vacancies in the system. The pink spheres and orange mesh represent oxygen vacancies and regions without oxygen vacancies, respectively. As shown in the figure, the distribution of oxygen vacancies changes over time, indicating stable oxygen migration. Moreover, the distance between oxygen vacancies, indicated by pink bonds, is approximately 0.6 nm, revealing that they can be found in different unit cells. In other words, two oxygen vacancies cannot exist within the same unit cell, as this would lead to crystal dislocation and disruption of the crystal order.

Table 2 presents activation energies, $E_a$, for $PrBa_{0.75}Sr_{0.25}Co_2O_{5.5}$, $PrBa_{0.75}Ca_{0.25}Co_2O_{5.5}$, $PrBa_{0.75}Na_{0.25}Co_2O_{5.375}$, and $PrBaCo_2O_{5.5}$ include 256 supercells in the *a–b* plane and along the *c*-axis. Moreover, this table compares the computed results in the current research with previous MD and experimental data. Intercomparison of the activation energy for $PrBaCo_2O_{5.5}$ in the *a–b* plane with values reported by MD simulations for $PrBaCo_2O_{5.5}$ [42] and experimental results for $PrBaCo_2O_{5.\delta}$ [63] reveals good agreement. The difference between the MD-calculated data in this work and the experimental values is attributed to variations in oxygen vacancy concentration. In experiments, accurately measuring the vacancy concentration is challenging; thus, δ is often reported as an unknown deviation from the ideal oxygen content and is not exactly equal to 0.5. This leads to discrepancies when compared with MD data, although the results remain relatively close. Moreover, the data show that doping with $Sr^{2+}$, $Ca^{2+}$, and $Na^{+}$ ions decreases the activation energy in both the *a–b* plane and along the *c*-axis. The effectiveness of the dopant ions in reducing activation energy follows the sequence: $Na^{+} > Sr^{2+} > Ca^{2+}$. Doping $Na^{+}$ into the $Ba^{2+}$ sublattice decreases the activation energy in the *a–b* plane and along the *c*-axis by 11% and 35%, respectively, compared to $PrBaCo_2O_{5.5}$.

**Table 2:** Comparison of activation energies for $PrBa_{0.75}Sr_{0.25}Co_2O_{5.5}$, $PrBa_{0.75}Ca_{0.25}Co_2O_{5.5}$, $PrBa_{0.75}Na_{0.25}Co_2O_{5.375}$, and $PrBaCo_2O_{5.5}$ in the *a–b* plane and along the *c*-axis calculated in the current study with previous MD and electrical conductivity relaxation (ECR) experimental results.

| Sample | Activation energy, $E_a$, (eV) | | Method | Reference |
|---|---|---|---|---|
| | In *a-b* plane | Along *c*-axis | | |
| $PrBa_{0.75}Sr_{0.25}Co_2O_{5.5}$ | 0.2977 | 0.2923 | Computational, MD | This work |
| $PrBa_{0.75}Ca_{0.25}Co_2O_{5.5}$ | 0.3209 | 0.2936 | Computational, MD | This work |
| $PrBa_{0.75}Na_{0.25}Co_2O_{5.375}$ | 0.3079 | 0.2634 | Computational, MD | This work |
| $PrBaCo_2O_{5.5}$ | 0.3491 | 0.4079 | Computational, MD | This work |
| $PrBaCo_2O_{5.5}$ | 0.3500 | NULL | Computational, MD | [42] |
| $PrBaCo_2O_{5.\delta}$ | 0.4800 | NULL | Experimental, ECR | [63] |

### 3.3. Oxygen diffusivity in $PrBaCo_{(2-y)}B'_yO_{5+\delta}$: y=0.25 and Co-Site Doping

Results for the double perovskite $PrBaCo_{(2-y)}B'_yO_{5+\delta}$, with y = 0.25 and B′ = Fe, Cr, Mn, Ni, Al, and Zn as dopant ions at the $Co^{3+}$ sites, are presented in this section. Accordingly, six doped structures including 256 supercells, are studied: $PrBaCo_{1.75}Fe_{0.25}O_{5.5}$, $PrBaCo_{1.75}Cr_{0.25}O_{5.5}$, $PrBaCo_{1.75}Mn_{0.25}O_{5.5}$, $PrBaCo_{1.75}Ni_{0.25}O_{5.5}$, $PrBaCo_{1.75}Al_{0.25}O_{5.5}$, and $PrBaCo_{1.75}Zn_{0.25}O_{5.375}$. The RDF diagrams of $PrBaCo_{1.75}Fe_{0.25}O_{5.5}$ at 873 K and 1323 K are compared in Fig. 3(a). Moreover, the RDF diagrams of other $Co^{3+}$ sublattice-doped double perovskites are also compared with each other in Fig. S6 of the supplementary material. All diagrams display sharp and well-defined peaks, suggesting the presence of a stable solid phase throughout the examined temperature range and the absence of crystallographic defects. Additionally, Fig. S7 compares the temporal evolution of internal pressure in these six doped double perovskites at 1323 K with that of $PrBaCo_2O_{5.5}$. The results show that the internal pressure in the doped systems fluctuates between −0.84 and +0.84 GPa, with an average value close to 0 Pa. These observations indicate that doping with $Fe^{3+}$, $Cr^{3+}$, $Mn^{3+}$, $Ni^{3+}$, $Al^{3+}$, and $Zn^{2+}$ neither significantly elevates internal pressure nor promotes crystallographic dislocations nor compromises the thermal and structural stability of the material.

Fig. 3(b) illustrates the time-dependent variation in MSD of all ions in $PrBaCo_{1.75}Fe_{0.25}O_5$. The results are presented for simulations at 1273 K, and for both diffusion in the *a–b* plane and along the *c*-axis. Consistent with trends observed for the case of doping at the $Ba^{2+}$ sites, MSD values in the *a–b* plane are consistently greater than those along the *c*-direction for every ion type. Only oxygen ions display clear diffusive behavior, as evidenced by the linear increase in their MSD over time. In contrast, the MSDs of

the remaining ions remain almost unchanged, aside from minor thermal fluctuations. A similar diffusion behavior is observed in the doped $PrBaCo_{1.75}Cr_{0.25}O_{5.5}$, $PrBaCo_{1.75}Mn_{0.25}O_{5.5}$, $PrBaCo_{1.75}Ni_{0.25}O_{5.5}$, $PrBaCo_{1.75}Al_{0.25}O_{5.5}$, and $PrBaCo_{1.75}Zn_{0.25}O_{5.375}$ across all investigated temperatures. The only difference is in the slope of the oxygen ion MSD curve, which is distinct for each composition and temperature.

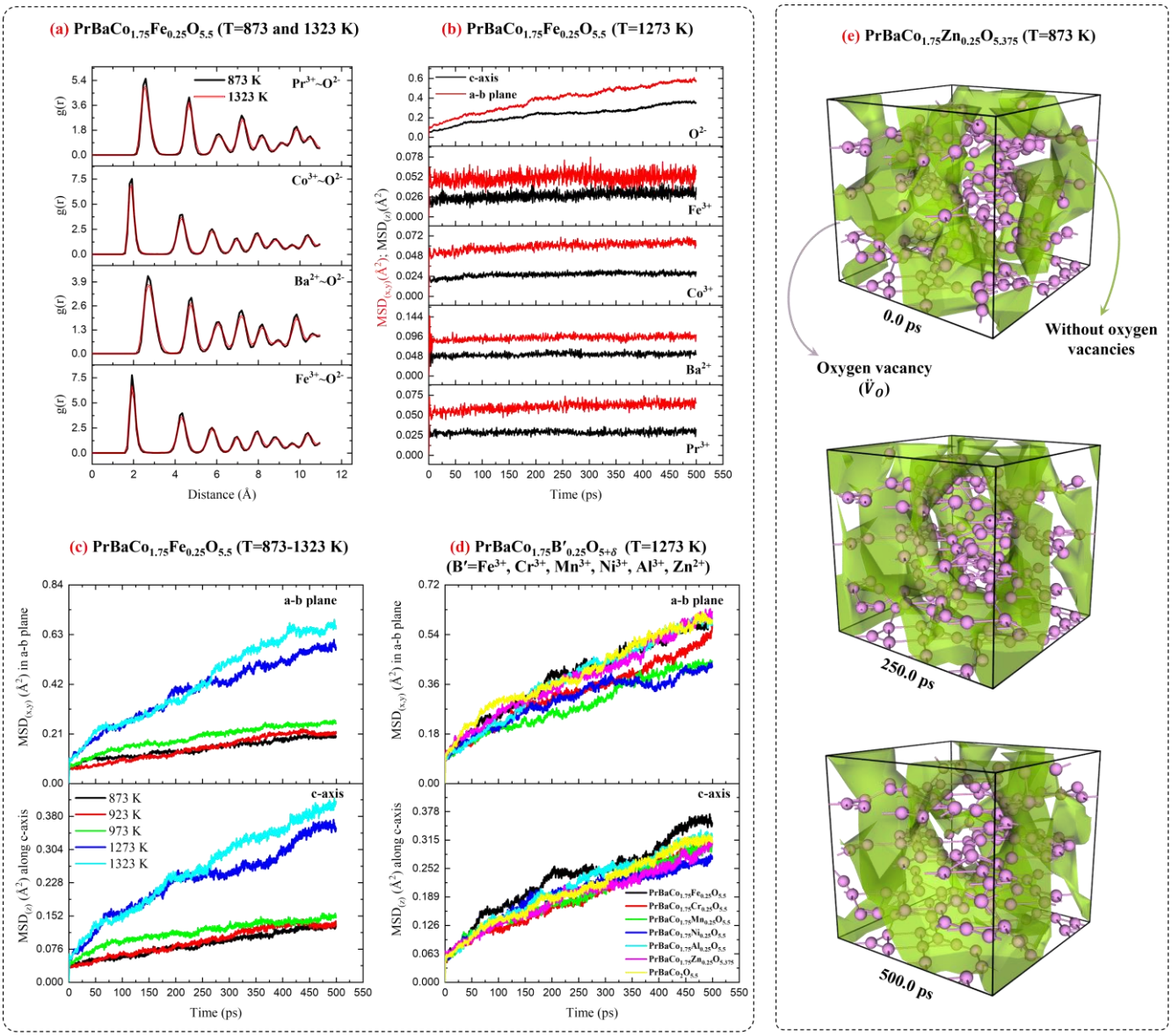


**Fig. 3** (a) The RDF diagrams of $PrBaCo_{1.75}Fe_{0.25}O_{5.5}$ at 873 K (black line) and 1323 K (red line). (b) The time-dependent variation in MSD of all ions in $PrBaCo_{1.75}Fe_{0.25}O_5$ including 256 supercells at 1273 K. (c) The temporal variations of MSD related to the oxygen ion in $PrBaCo_{1.75}Fe_{0.25}O_5$ at different temperatures. (d) The temporal variations of MSD related to the oxygen ion in double perovskite $PrBaCo_{1.75}B'_{0.25}O_{5+\delta}$, where B′ = Fe, Cr, Mn, Ni, Al, and Zn at 1273 K. (e) The snapshots of the $PrBaCo_{1.75}Zn_{0.25}O_{5.375}$ configurations at 0.0, 250, and 500 ps include both oxygen vacancies (pink spheres) and regions without oxygen vacancies (green mesh) at 873 K

The temporal variation of the MSD of oxygen ions in $PrBaCo_{1.75}Fe_{0.25}O_5$ at different temperatures between 873 and 1323 K is shown in Fig. 3(c). The figure clearly shows that increasing the temperature enhances both the diffusivity and the oxygen diffusion coefficient. A similar trend is observed in the other doped double perovskite $PrBaCo_{1.75}B'_{0.25}O_{5+\delta}$. The results in Fig. 3(d) illustrate the time-dependent variation in MSD related to the oxygen ion diffusion in $PrBaCo_{1.75}Fe_{0.25}O_{5.5}$, $PrBaCo_{1.75}Cr_{0.25}O_{5.5}$, $PrBaCo_{1.75}Mn_{0.25}O_{5.5}$, $PrBaCo_{1.75}Ni_{0.25}O_{5.5}$, $PrBaCo_{1.75}Al_{0.25}O_{5.5}$, $PrBaCo_{1.75}Zn_{0.25}O_{5.375}$, and $PrBaCo_2O_{5.5}$, at 1273 K. The figure shows that the oxygen ion diffusion is different for different dopants at the $Co^{3+}$ sites. In general, the ion diffusion along the *c*-axis is less influenced by the doping.

Fig. 3(e) depicts the snapshots of the $PrBaCo_{1.75}Zn_{0.25}O_{5.375}$ configuration from 0.0 to 500.0 ps at 873 K. The figure reveals two main regions: those containing oxygen vacancies, illustrated by pink spheres, and those without oxygen vacancies, specified by the green mesh. This figure shows the distribution of oxygen vacancies in the system changes over time, validating the MSD diagrams. Moreover, the minimum distance between oxygen vacancies is approximately 0.6 nm, which indicates that two oxygen vacancies cannot appear within the same unit cell, as previously observed for doping at the $Ba^{2+}$ site. In summary, doping at both $Ba^{2+}$ and $Co^{3+}$ sites do not result in the appearance of two oxygen vacancies within a single unit cell, thereby preserving the crystalline order of the system and preventing dislocations.

To further investigate the effect of doping at the $Co^{3+}$ sites on oxygen diffusivity, the $E_a$ for the doped double perovskites is calculated and presented in Table 3. The values are given separately for diffusion in the *a–b* plane and along the *c*-axis. Interestingly, the activation energy for diffusion along the *c*-axis decreases upon doping, with the largest reduction observed for the $Fe^{3+}$ dopant. However, the trend in the *a–b* plane is more complex. All dopants, except $Cr^{3+}$,$Fe^{3+}$, and $Al^{3+}$ reduce the activation energy in the *a–b* plane, thus enhancing oxygen diffusivity. The ability of the dopant ions to reduce the activation energy in the *a–b* plane follows the order: $Zn^{2+} > Ni^{3+} > Mn^{3+}$. Doping with $Al^{3+}$ results in only a slight reduction in activation energy, while $Fe^{3+}$ has a negligible effect on the activation energy for diffusion in the *a–b* plane. Doping with $Cr^{3+}$ increases the activation energy of $PrBaCo_2O_{5.5}$ in the *a–b* plane by more than 12%. These phenomena and the response of $PrBaCo_2O_{5.5}$ to doping at $Co^{3+}$ sites originate from orbital manipulation of the system by foreign dopant ions. Doped transition metal ions, through their interaction with oxygen ions, alter the electronic orbitals and influence diffusivity.

**Table 3:** The activation energy of $PrBaCo_{1.75}Fe_{0.25}O_{5.5}$, $PrBaCo_{1.75}Cr_{0.25}O_{5.5}$, $PrBaCo_{1.75}Mn_{0.25}O_{5.5}$, $PrBaCo_{1.75}Ni_{0.25}O_{5.5}$, $PrBaCo_{1.75}Al_{0.25}O_{5.5}$, $PrBaCo_{1.75}Zn_{0.25}O_{5.375}$, and $PrBaCo_2O_{5.5}$, in the *a–b* plane and along the *c*-axis.

| Sample | Activation energy, $E_a$, (eV) | |
|---|---|---|
| | In *a-b* plane | Along *c*-axis |
| $PrBaCo_{1.75}Fe_{0.25}O_{5.5}$ | 0.3491 | 0.2829 |
| $PrBaCo_{1.75}Cr_{0.25}O_{5.5}$ | 0.3923 | 0.3240 |
| $PrBaCo_{1.75}Mn_{0.25}O_{5.5}$ | 0.3389 | 0.2930 |
| $PrBaCo_{1.75}Ni_{0.25}O_{5.5}$ | 0.3206 | 0.3814 |
| $PrBaCo_{1.75}Al_{0.25}O_{5.5}$ | 0.3470 | 0.3052 |
| $PrBaCo_{1.75}Zn_{0.25}O_{5.375}$ | 0.3060 | 0.2975 |
| $PrBaCo_2O_{5.5}$ | 0.3491 | 0.4079 |

### 3.4. Oxygen diffusivity in $PrBa_{(1-x)}A'_xCo_{(2-y)}B'_yO_{5+\delta}$: x=y=0.125 and Dual-Site Doping

Based on the results presented in Sections 3.2 and 3.3, doping with $Na^+$ at the $Ba^{2+}$ sites and with $Zn^{2+}$ at the $Co^{3+}$ sites are the appropriate choices to improve oxygen diffusivity and reduce the activation energy of the double perovskite $PrBaCo_2O_{5.5}$. This section investigates how dual-site doping with these ions affects the oxygen diffusivity of $PrBaCo_2O_{5.5}$. To this end, the crystal stability in the solid phase, ionic diffusion process, and diffusion activation energy in 256 supercells of $PrBa_{0.875}Na_{0.125}Co_{1.875}Zn_{0.125}O_{5.375}$ were studied and compared with the results of $PrBa_{0.75}Na_{0.25}Co_2O_{5.375}$, $PrBaCo_{1.75}Zn_{0.25}O_{5.375}$, and $PrBaCo_2O_{5.5}$.

The RDF diagrams of the dual-site doped $PrBa_{0.875}Na_{0.125}Co_{1.875}Zn_{0.125}O_{5.375}$ at 873 K and 1323 K are presented and compared in Fig. S8. The diagrams are characterized by sharp and well-defined peaks, confirming the presence of a stable solid phase throughout the examined temperature range and the absence of crystallographic defects. The time-dependent variations of internal pressure in all four structures are presented in Fig. S9. It is evident from the figure that dual-site doping does not significantly impact the internal pressure of the structure, as the pressure fluctuates around zero with an amplitude of approximately 0.84 GPa. Therefore, it is concluded that $PrBa_{0.875}Na_{0.125}Co_{1.875}Zn_{0.125}O_{5.375}$ is structurally and thermally stable within the studied temperature range.

The variations of the MSD of all the involved ions in $PrBa_{0.875}Na_{0.125}Co_{1.875}Zn_{0.125}O_{5.375}$ at 1273 K are illustrated in Fig. S10. The results are presented for diffusion in the *a–b* plane and along the *c*-axis. The following observations are made: (i) diffusion is more pronounced in the *a–b* plane than along the *c*-axis;

(ii) only oxygen ions exhibit significant diffusion; (iii) the lack of diffusion of $Na^+$ and $Zn^{2+}$ ions, commonly used as charge carriers in Na-air and Zn-air batteries, may limit the cyclability of these battery systems if these doped double perovskites are used as a catalyst. The evolution of the MSD of oxygen ions over time in $PrBa_{0.875}Na_{0.125}Co_{1.875}Zn_{0.125}O_{5.375}$ at different temperatures between 873 and 1323 K is shown in Fig. S11. The results are presented for the diffusion in the *a–b* plane and along the *c*-axis. Consistent with the observations made in previous sections, increasing the temperature up to 1273 K generally enhances oxygen diffusivity. However, a further increase from 1273 K to 1323 K leads to a slight decrease in oxygen diffusion.

To further investigate the effect of dual-site doping, the $E_a$ for 256 supercells of $PrBa_{0.875}Na_{0.125}Co_{1.875}Zn_{0.125}O_{5.375}$ is presented in Table 4 and compared with the results for $PrBa_{0.75}Na_{0.25}Co_2O_{5.375}$, $PrBaCo_{1.75}Zn_{0.25}O_{5.375}$, and $PrBaCo_2O_{5.5}$. The dual-site doped $PrBa_{0.875}Na_{0.125}Co_{1.875}Zn_{0.125}O_{5.375}$ has the lowest activation energy for diffusion in both directions. It is concluded that simultaneous doping with $Na^+$ at the $Ba^{2+}$ sites and with $Zn^{2+}$ at the $Co^{3+}$ sites improves oxygen conductivity and reduces the activation energy of the double perovskite $PrBaCo_2O_{5.5}$, and therefore, $PrBa_{0.875}Na_{0.125}Co_{1.875}Zn_{0.125}O_{5.375}$ can be an efficient catalyst for LABs.

**Table 4:** The activation energy of $PrBa_{0.875}Na_{0.125}Co_{1.875}Zn_{0.125}O_{5.375}$, $PrBa_{0.75}Na_{0.25}Co_2O_{5.375}$, $PrBaCo_{1.75}Zn_{0.25}O_{5.375}$, and $PrBaCo_2O_{5.5}$ in the *a–b* plane and along the *c*-axis.

| Sample | Activation energy, $E_a$, (eV) | |
|---|---|---|
| | In *a*-*b* plane | Along *c*-axis |
| $PrBa_{0.875}Na_{0.125}Co_{1.875}Zn_{0.125}O_{5.37}$ | 0.2636 | 0.2371 |
| $PrBa_{0.75}Na_{0.25}Co_2O_{5.375}$ | 0.3079 | 0.2634 |
| $PrBaCo_{1.75}Zn_{0.25}O_{5.375}$ | 0.3060 | 0.2975 |
| $PrBaCo_2O_{5.5}$ | 0.3491 | 0.4079 |

### 3.5. Oxygen and Lithium Diffusivity in $Li_{0.2\xi}$-doped $PrBa_{(1-\xi)}Co_2O_{5.5}$: $\xi$=0.0625 and Interstitial-Site Doping

The effect of $Li^+$ ion doping at the interstitial lattice sites of $PrBaCo_2O_{5.5}$ is investigated in this section. To this end, MD simulations were conducted on the 256 supercells of $Li_{0.125}$-doped $PrBa_{0.9375}Co_2O_{5.5}$. The RDF diagrams at 873 K and 1323 K are presented and compared in Fig. 4(a). These diagrams exhibit sharp and well-defined peaks, indicating a structurally stable solid phase throughout the studied temperature range, with no signs of crystallographic defects. Furthermore, the RDF plots do not show a

distinct peak corresponding to the $Li^+$~$O^{2-}$ distance, confirming that $Li^+$ ions occupy interstitial lattice sites rather than substituting existing ions and migrate through interstitial diffusion pathways. The time evolution of internal pressure in $Li_{0.125}$-doped $PrBa_{0.9375}Co_2O_{5.5}$ is shown in Fig. S12, alongside that of undoped $PrBaCo_2O_{5.5}$ for comparison. The data indicate that $Li^+$ ion doping exerts a negligible influence on the internal pressure, which fluctuates around zero with a typical amplitude of about 0.81 GPa.

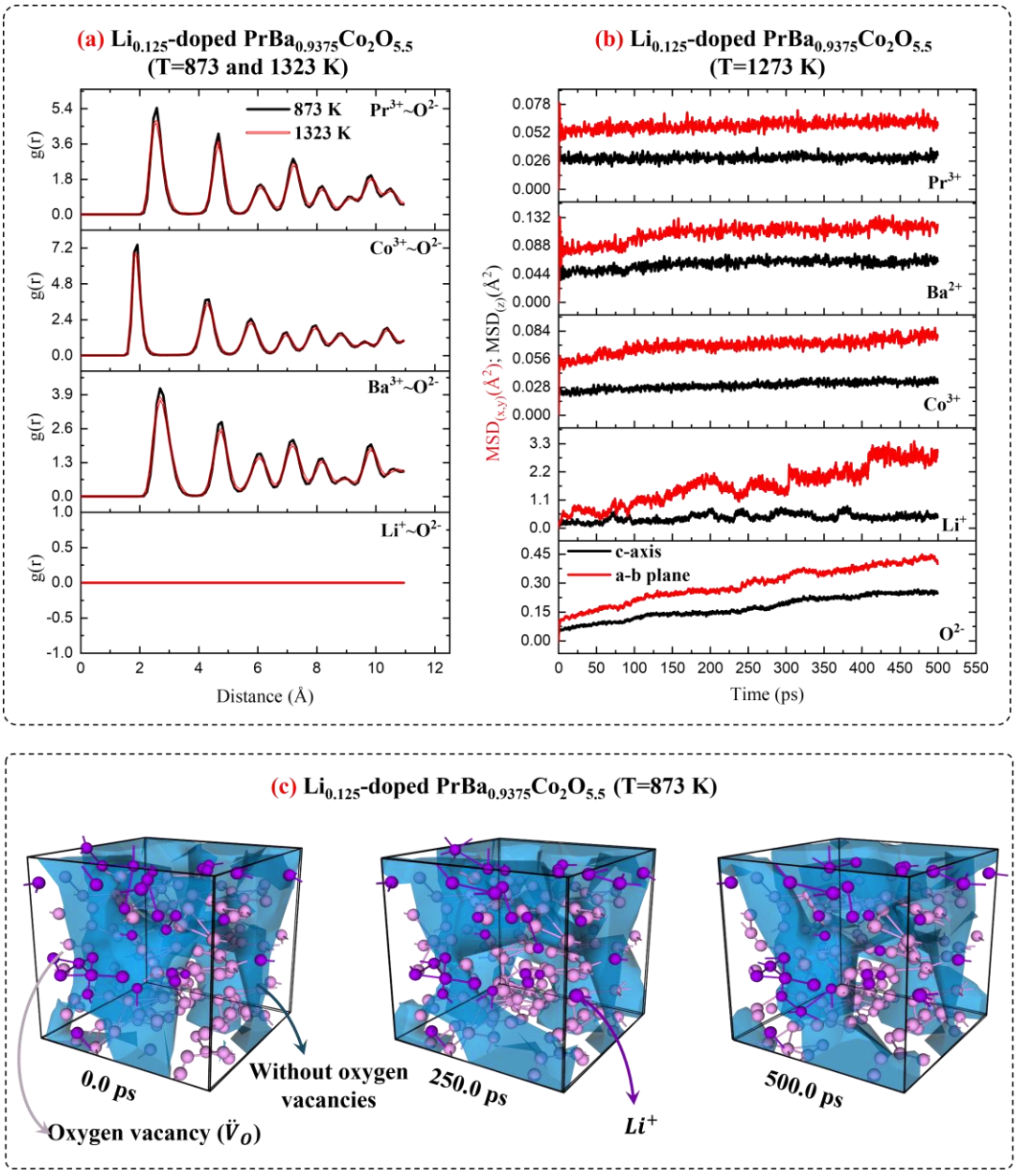


**Fig. 4** (a) The RDF diagrams of 256 supercells of $Li_{0.125}$-doped 256 $PrBa_{0.9375}Co_2O_{5.5}$ at 873 K (black line) and 1323 K (red line). (b) The temporal variations of MSD related to all ions in 256 $Li_{0.125}$-doped 256 $PrBa_{0.9375}Co_2O_{5.5}$ at 1273 K. (c) The snapshots of $Li_{0.125}$-doped 256 $PrBa_{0.9375}Co_2O_{5.5}$ configurations at 0.0, 250, and 500 ps include both oxygen vacancies (pink spheres), $Li^+$ (purple spheres) and regions without oxygen vacancies (blue mesh) at 873 K.

The temporal variations of the MSD for all ion types in $Li_{0.125}$-doped$PrBa_{0.9375}Co_2O_{5.5}$ at 1273 K are presented in Fig. 4(b) for both diffusion in the *a–b* plane and along the *c*-axis. As evident from the figure, $Pr^{3+}$ and $Co^{3+}$ ions do not exhibit diffusion, as their MSD values remain nearly constant over time. Interestingly, even $Ba^{2+}$ ions show no sign of diffusion despite the presence of $\acute{V}_{Ba}$ in the structure. However, both $Li^+$ and $O^{2-}$ ions exhibit diffusion, as indicated by the linear increase of their MSD curves over time. For both ion types, the diffusion coefficient is higher in the *a–b* plane than along the *c*-axis. It is worth noting that lithium doping does not hinder oxygen diffusivity within the structure.

Fig. 4(c) compares the snapshots of the system at 0.0, 250.0, and 500.0 ps at 873 K, providing visual evidence of oxygen vacancy mobility and $Li^+$ diffusivity in the simulation. Oxygen vacancies, $Li^+$, and regions without oxygen vacancies are illustrated by pink spheres, purple spheres, and blue mesh, respectively. The figure shows that the distributions of oxygen vacancies and $Li^+$ change over time, highlighting the dual $O^{2-}$ and $Li^+$ ionic mobility in the system. Moreover, the minimum distances between oxygen vacancies-oxygen vacancies and $Li^+$-$Li^+$ are approximately 0.6 nm and 0.8 nm, respectively. These distances indicate that oxygen vacancies and $Li^+$ are located in different unit cells, ensuring a dislocation-free crystal. Consequently, doping at the $Ba^{2+}$ and $Co^{3+}$ sites or interstitial doping cannot provide the conditions necessary for two oxygen vacancies to exist within the same unit cell.

The observation that, in addition to $O^{2-}$, interstitially doped $Li^+$ exhibit diffusivity, while $Ba^{2+}$ ions remain immobile, is a significant finding for LABs, as it highlights the synergistic effect of both $O^{2-}$ and $Li^+$ mobility in $Li_{0.125}$-doped $PrBa_{0.9375}Co_2O_{5.5}$. Consequently, this material can serve as a suitable catalyst in LABs, which contributes to improved chargeability and enhanced cyclability. To further validate this observation, the temporal evolutions of the MSD for $O^{2-}$, $Li^+$, and $Ba^{2+}$ at five different temperatures ranging from 873 K to 1323 K are presented in Fig. 5.The absence of $Ba^{2+}$ diffusion across all studied temperatures is evident. In contrast, both $O^{2-}$ and $Li^+$ exhibit diffusion at all temperatures in both directions. Consistent with earlier findings, the diffusion is more pronounced in the *a–b* plane than along the *c*-axis and generally increases at higher temperatures.

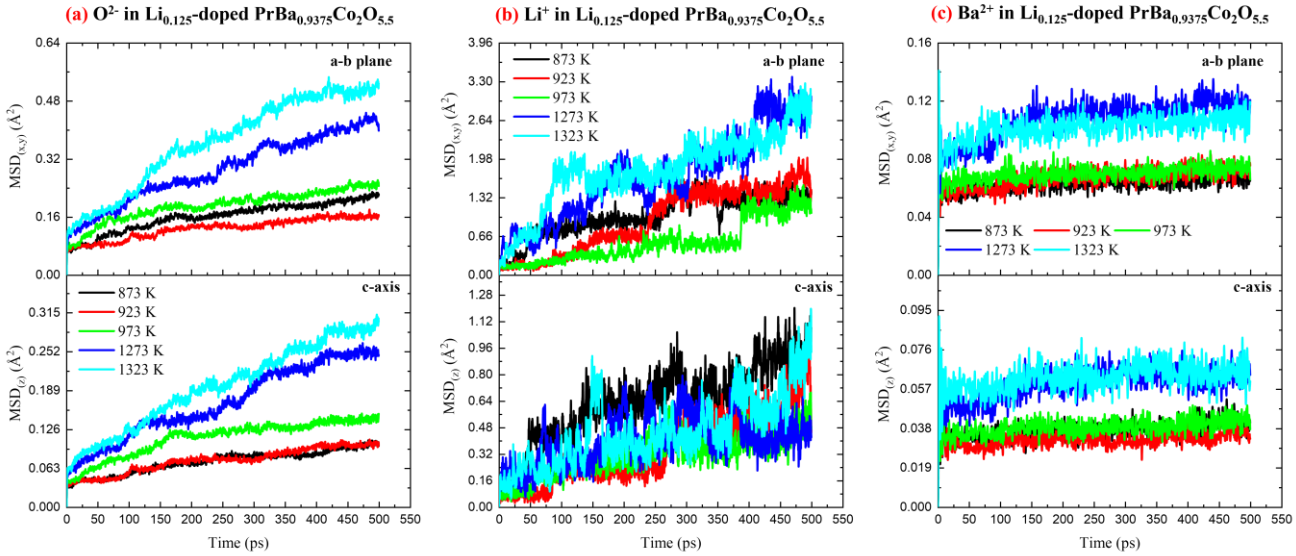


**Fig. 5** The temporal variations of MSD related to the (a) oxygen, (b) lithium, and (c) barium ions in 256 supercells of $Li_{0.125}$-doped $PrBa_{0.9375}Co_2O_{5.5}$ at different temperatures.

The oxygen and lithium $E_a$ for $Li_{0.125}$-doped $PrBa_{0.9375}Co_2O_{5.5}$ is presented in Table 5 and compared with the results for dual-site doped $PrBa_{0.875}Na_{0.125}Co_{1.875}Zn_{0.125}O_{5.37}$ and undoped $PrBaCo_2O_{5.5}$.. Regarding $O^{2-}$ diffusion, the activation energy in the *a–b* plane is lower than that along the *c*-axis for all three catalysts except $PrBa_{0.875}Na_{0.125}Co_{1.875}Zn_{0.125}O_{5.37}$. $Li_{0.125}$-doped $PrBa_{0.9375}Co_2O_{5.5}$ and dual-site doped $PrBa_{0.875}Na_{0.125}Co_{1.875}Zn_{0.125}O_{5.37}$ exhibit the lowest activation energy in the *a–b* plane and along the *c*-axis, respectively, and both demonstrate improved oxygen diffusivity in both directions compared to the undoped $PrBaCo_2O_{5.5}$.

A key feature of $Li_{0.125}$-doped $PrBa_{0.9375}Co_2O_{5.5}$ is its $Li^+$ diffusivity, which occurs with low activation energy in both the *a–b* plane and along the c-axis, making it a promising candidate for use as a catalyst in LABs. Moreover, evaluation of $Li_{0.125}$-doped $PrBa_{0.9375}Co_2O_{5.5}$ and $PrBa_{0.875}Na_{0.125}Co_{1.875}Zn_{0.125}O_{5.37}$ for Li-air, Na–air, and Zn–air batteries (see Table 5), from the perspective of oxygen and charge carrier mobility, reveals that only $Li_{0.125}$-doped $PrBa_{0.9375}Co_2O_{5.5}$ offers both $O^{2-}$ and $Li^+$ diffusion. This outcome is a positive effect for Li-air batteries, as it can facilitate the formation and decomposition of discharge products ($Li_2O_2$ and $Li_2O$). However, $Na^+$ and $Zn^{2+}$ cannot diffuse in either perovskite, indicating that these catalysts cannot effectively facilitate the charge/discharge rate in Na–air and Zn–air batteries, respectively.

**Table 5:** The activation energy of $Li_{0.125}$-doped $PrBa_{0.9375}Co_2O_{5.5}$, $PrBa_{0.875}Na_{0.125}Co_{1.875}Zn_{0.125}O_{5.37}$, and $PrBaCo_2O_{5.5}$ in the *a*–*b* plane and along the *c*-axis.

| Sample | Activation energy, $E_a$, (eV) | | | | Diffusivity of important species for Li-air, Na-air, and Zn-air batteries | | | |
|---|---|---|---|---|---|---|---|---|
| | $O^{2-}$ ion | | $Li^+$ ion | | | | | |
| | *a*-*b* plane | *c*-axis | *a*-*b* plane | *c*-axis | $O^{2-}$ | $Li^+$ | $Na^+$ | $Zn^{2+}$ |
| $Li_{0.125}$-doped $PrBa_{0.9375}Co_2O_{5.5}$ | 0.2528 | 0.3560 | 0.1788 | 0.1579 | ☺✓ | ☺✓ | ☹× | ☹× |
| $PrBa_{0.875}Na_{0.125}Co_{1.875}Zn_{0.125}O_{5.37}$ | 0.2636 | 0.2371 | NULL | NULL | ☺✓ | ☹× | ☹× | ☹× |
| $PrBaCo_2O_{5.5}$ | 0.3491 | 0.4079 | NULL | NULL | ☺✓ | ☹× | ☹× | ☹× |

## 4. Outlook and challenges

Offshore renewable energy is a rapidly growing sector of sustainable green energy that plays a crucial role in reducing $CO_2$ emissions [64]. Offshore power plants are becoming increasingly important and is now a key part of major policy plans, as demonstrated by the European Commission's strategy to support offshore renewable energy and help the EU meet its 2030 carbon emission reduction targets and achieve climate neutrality by 2050 [65,66]. Offshore power plants harness energy through various methods and sources, including offshore and floating wind turbines, wave and tidal power, and, more recently, floating photovoltaic systems [67,68]. Fig. 6 illustrates offshore and floating wind turbines for harvesting energy from the environment. However, the development of renewable and green energy sources, along with the seamless integration of the generated electrical energy into power grids, is becoming increasingly challenging due to their intermittency [69,70].

High-capacity energy storage devices offer a promising strategy to store surplus energy during periods of low demand and release it during peak times [71]. Nonetheless, this approach requires cost-effective and high-capacity energy storage systems capable of supplying power for several hours. Fig. 7 compares the theoretical capacity and voltage of conventional and state-of-the-art batteries as energy storage devices, which offer constant voltage during discharge operation. The intercomparison of batteries in this figure reveals that LABs, with high theoretical energy density, suitable operating voltage ranges, and low manufacturing costs, hold promise for scaling up and integrating into the offshore power plant sector as energy storage solutions.

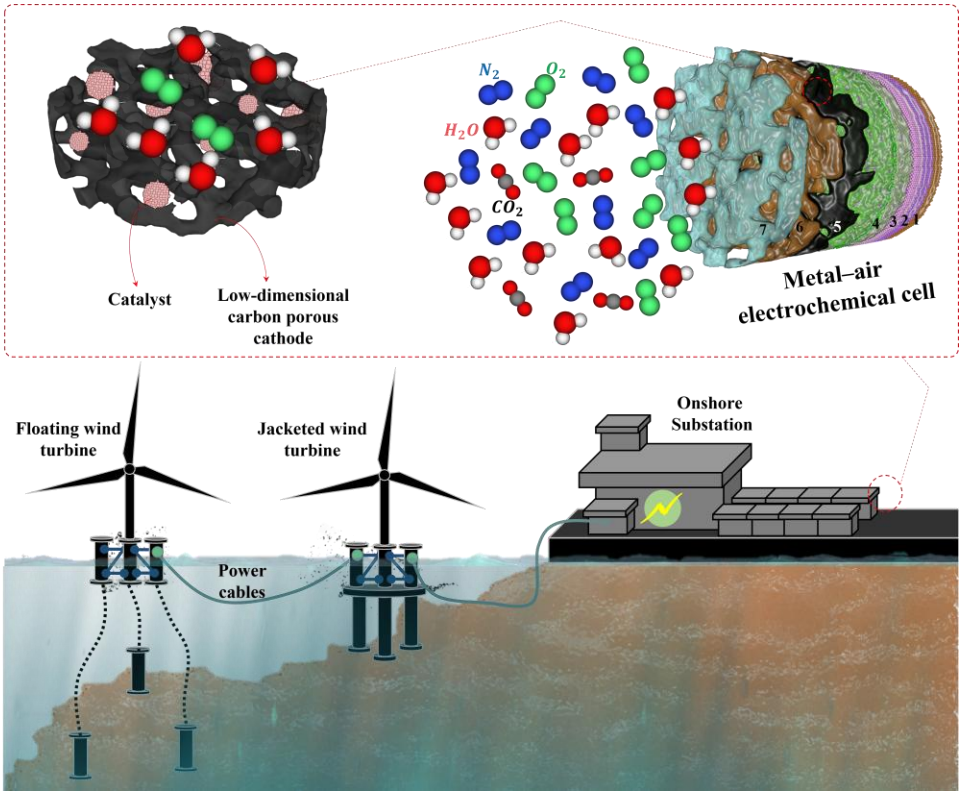


**Fig. 6** The general schematic of offshore wind power plants includes: floating and jacketed wind turbines, an onshore substation, and metal-air batteries as their energy storage systems. Power generated by floating and jacketed wind turbines is transferred via power cables to an onshore substation and stored in metal-air batteries. During the charging process, metal-air batteries draw oxygen gas from the air; however, vapor molecules also diffuse into the cathode due to their similar kinetic radius to oxygen, thereby reducing the cycling lifetime. The metal-air electrochemical cell includes: (1) Anode current collector, (2) Metallic anode such as lithium, sodium, and zinc, (3) Solid-electrolyte-interphase layer, (4) Electrolyte and separator, (5) Air-cathode and catalysts, (6) Cathode current collector, and (7) Oxygen-selective membrane.

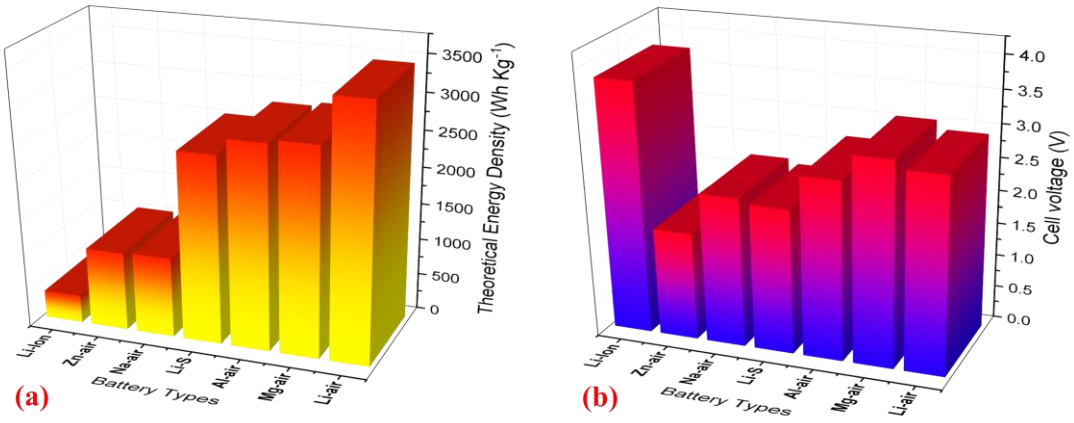


**Fig. 7** Comparison of (a) theoretical energy capacity and (b) cell voltage for conventional and state-of-the-art batteries. The data used to plot this figure were collected from references [72,73] and were originally plotted by the authors in the current work.

Fig. 6 and Fig. 7 illustrate that metal-air batteries can serve as promising candidates for storing electricity generated by offshore power plants due to their unique advantages, particularly their high theoretical energy density. However, in this application, the risk of $H_2O$ diffusion into the electrochemical cell increases due to the high evaporation rate of water in these environments and the similar kinetic radius of $H_2O$ molecules to that of oxygen gas ($O_2$) [56,74]. If $H_2O$ penetrates the cell, it can react with lithium to form undesirable byproducts, such as LiOH [15]. These side-products are difficult to decompose, and their continuous formation and accumulation on the cathode surface hinder the efficiency of ORR/OER in discharge/charge processes, ultimately degrading cell performance.

To address these challenges, ORR/OER catalysts and oxygen-selective membranes have been proposed to enhance catalytic activity during discharge/charge processes and selectively extract $O_2$ from the environment [9,75]. The results presented in this article contribute to the advancement of LABs by improving oxygen diffusivity through the use of double perovskite oxides as catalysts and identifying effective methods for enhancing ionic diffusion. This study demonstrates that $Li_{0.125}$-doped $PrBa_{0.9375}Co_2O_{5.5}$ is a promising candidate for improving dual $Li^+$ and $O^{2-}$ mobility, which supports ORR/OER catalytic activity. However, in offshore and onshore environments, the high concentration of $H_2O$ presents a significant limitation that needs to be carefully addressed. Conventionally, oxygen-selective membranes are employed to separate $O_2$ from air [75]; however, $H_2O$ (0.28 nm) can also diffuse to the air cathode due to its similar kinetic energy to $O_2$ (0.36 nm) [74], leading to the formation of LiOH. Under these conditions, different solutions are required to ensure stable operation under high humidity.

The combination of a water-splitting catalyst [76], an anaerobic cathodic electrode [77], and a bio-inspired oxygen-selective-membrane [78] represents a promising strategy for enabling stable charge/discharge operations in offshore or onshore environments characterized by high humidity. Adding additional water-splitting catalysts, such as sulfur- and nitrogen-doped low-dimensional carbon allotropes mixed with metal and transition metal oxide materials in the air-cathode, is a promising approach to split infiltrated $H_2O$ and convert it to $O_2$. Anaerobic cathodic electrodes, such as copper(II) oxide (CuO), provide the necessary conditions to operate under anaerobic environments by enabling dual operation modes: metal-air for aerobic and metal-ion for anaerobic conditions. Bio-inspired oxygen-selective-membranes, created by combining typical oxygen-selective-membranes with $Co_2Fe$-NC catalyst (which inspired by fish gills), can extract $O_2$ from high-humidity conditions to ensure stable operation.

The achieved results in the current research and literature review reveal that LABs designed for offshore or onshore environments with high humidity require modifications on the cathode side. As illustrated in Fig. 8, a new air-cathode composite, two types of catalysts, and bio-inspired oxygen-selective-membranes, are necessary to ensure the lifetime and reliable operation of charge/discharge cycles. The air-cathode needs to be synthesized as a composite comprising sulfur- and nitrogen-doped low-dimensional porous carbon allotropes [9,79,80] and metal oxides as the matrix, with transition metal oxides and $Li_{0.125}$-doped $PrBa_{0.9375}Co_2O_{5.5}$ as additives. In this composite, the porous low-dimensional carbon allotropes provide the necessary space for the formation of discharge products ($Li_2O_2$ and $Li_2O$), offer good electronic conductivity, and are cost-effective. The sulfur and nitrogen doping enhances the electrochemical stability of the porous carbon by creating chemically resistant bonds with carbon atoms.

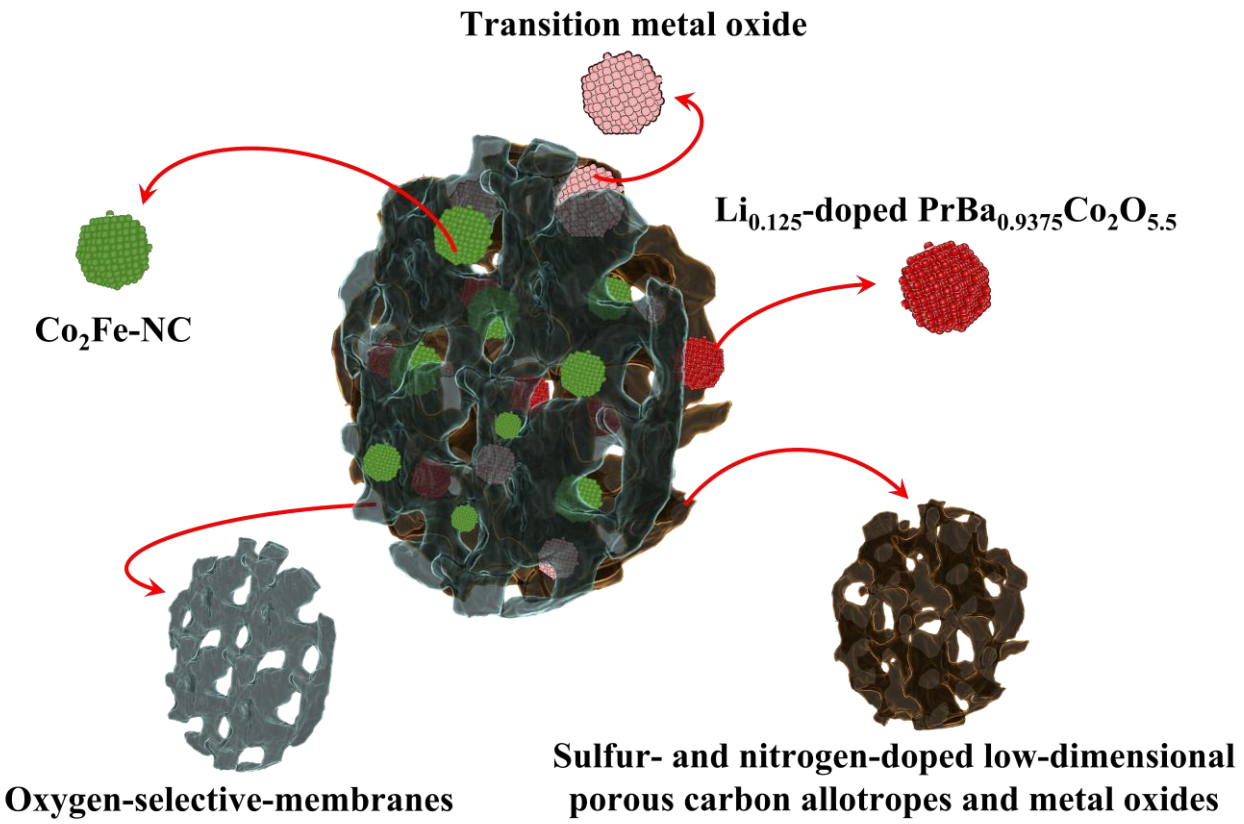


**Fig. 8** Promising air-cathode for metal-air batteries in offshore and onshore environments with high humidity. The air-cathode includes sulfur- and nitrogen-doped low-dimensional porous carbon allotropes and metal oxides as the matrix, transition metal oxide and $Li_{0.125}$-doped $PrBa_{0.9375}Co_2O_{5.5}$ as catalysts, and oxygen-selective-membranes decorated with $Co_2Fe$-NC catalysts.

Metal oxides also provide the necessary conditions for dual-mode operation of batteries, functioning as metal-air and metal-ion systems under aerobic and anaerobic conditions, respectively, depending on the concentration of $O_2$. Transition metal oxide catalysts assist in splitting the infiltrated $H_2O$ molecules within the air-cathode, thereby preventing the formation of LiOH. The $Li_{0.125}$-doped $PrBa_{0.9375}Co_2O_{5.5}$ catalyst enhances both $Li^+$ and $O^{2-}$ diffusivity, contributing to OER/ORR performance. Oxygen-selective-membranes decorated with $Co_2Fe$-NC catalysts further facilitate the selective transport of $O_2$ in high-humidity environments and help reduce the likelihood of LiOH side-product formation. As a result, the air-cathode can maintain continuous operation under humid conditions. However, these components need to be carefully engineered and assessed in terms of parameters such as weight, volume, cost, and durability to achieve practical feasibility and enable commercialization.

## 5. Conclusions

This study systematically investigated the effects of doping on the ionic diffusivity of the double perovskite $PrBaCo_2O_{5.5}$ at temperatures ranging from 873 K to 1323 K using MD simulations. Four distinct doping strategies were considered: (i) substitution at the $Ba^{2+}$ sites with $Sr^{2+}$, $Ca^{2+}$, and $Na^+$; (ii) substitution at the $Co^{3+}$ sites with $Fe^{3+}$, $Cr^{3+}$, $Mn^{3+}$, $Ni^{3+}$, $Al^{3+}$, and $Zn^{2+}$; (iii) dual-site doping at both $Ba^{2+}$ and $Co^{3+}$ sites with $Na^+$ and $Zn^{2+}$; and (iv) interstitial doping with $Li^+$ ions. In general, the doped double perovskites follow the formula $PrBa_{(1-x)}A'_xCo_{(2-y)}B'_yO_{5+\delta}$, where A′ = Sr, Ca, or Na and B′ = Fe, Cr, Mn, Ni, Al, or Zn, with $0 \leq x=y \leq 0.25$. Li was doped with a 0.125 concentration in interstitial sites.

The simulations have shown that all doped double perovskites remain thermally and structurally stable, retaining solid-phase integrity without any crystallographic defects or dislocations. Furthermore, all compositions exhibit anisotropic oxygen ion diffusivity, with diffusion generally more pronounced in the *a*–*b* plane than along the *c*-axis. As expected, increasing the temperature generally enhances the diffusion coefficients. In the case of $PrBa_{0.75}$(Sr, Ca, or Na)$_{0.25}Co_2B'_yO_{5+\delta}$, $Na^+$ doping at the $Ba^{2+}$ sites yield the most significant enhancement in the oxygen diffusion coefficient and the greatest reduction in activation energy, compared to doping with $Sr^{2+}$ or $Ca^{2+}$ at the same sites. Similarly, in $PrBaCo_{1.75}$(Fe, Cr, Mn, Ni, Al, or Zn)$_{0.25}O_{5+\delta}$, $Zn^{2+}$ doping at the $Co^{3+}$ sites resulted in the most pronounced improvements in oxygen diffusivity relative to doping with $Fe^{3+}$, $Cr^{3+}$, $Mn^{3+}$, $Ni^{3+}$, or $Al^{3+}$.

With knowledge of the suitability of $Na^+$ and $Zn^{2+}$ in promoting oxygen diffusivity, the dual-site doped composition $PrBa_{0.875}Na_{0.125}Co_{1.875}Zn_{0.125}O_{5.375}$ was examined. The outcomes show that, due to the synergistic effects of simultaneous doping at both $Ba^{2+}$ and $Co^{3+}$ sites, the resulting material exhibits even lower activation energy and a higher oxygen diffusion coefficient. These outcomes may originate from the orbital manipulation of oxygen by the dopant ions. The $PrBa_{0.875}Na_{0.125}Co_{1.875}Zn_{0.125}O_{5.375}$ does

not exhibit $Na^+$ or $Zn^{2+}$ diffusion, which may render it unsuitable as a catalyst for sodium–air and zinc–air batteries. However, its high oxygen diffusivity makes it a promising candidate as an efficient catalyst for LABs, since $Na^+$ or $Zn^{2+}$ diffusivity is not required for these batteries.

Doping of interstitial sites with $Li^+$ results in the formation of $Li_{0.125}$-doped $PrBa_{0.9375}Co_2O_{5.5}$ and offers not only $O^{2-}$ diffusivity comparable to that of the dual-site doped perovskite in the a–b plane, but also enables efficient $Li^+$ diffusion with low activation energy in both the a–b plane and along the c-axis. This dual $Li^+$ and $O^{2-}$ mobility is a significant finding, as it promotes the formation and decomposition of discharge products ($Li_2O$ and $Li_2O_2$) at an enhanced rate, thereby improving the performance of LABs in a dry environment. However, for offshore environments with high humidity, the presence of novel air-cathodes with two catalysts is necessary to ensure stable operation. For these humid environments, an air-cathode composite can be synthesized from doped porous carbon allotropes and metal oxides as the matrix, combined with transition metal oxides and $Li_{0.125}$-doped $PrBa_{0.9375}Co_2O_{5.5}$ as catalysts, and a bio-inspired oxygen-selective-membrane. Such an air-cathode can operate as a metal-air and a metal-ion system under aerobic and anaerobic conditions, respectively, while mitigating the ingress of $H_2O$ into cells, thereby extending cycle life in humid environments.

## Author Contributions

**Sasan Rezaee**: Conceptualization, Project administration, Supervision, Methodology, Data curation, Formal analysis, Investigation, Software, Validation, Visualization, writing-original draft, and writing-review and editing. **Hossein Darban**: Conceptualization, Project administration, Supervision, Investigation, Validation, Writing-original draft, and Writing-review and Editing. **Nilüfer Ertekin**: Investigation, Methodology, Software, Writing-original draft, and Writing-review and editing. **Fatemeh Mohammad Dezashibi**: Investigation, Visualization, and Writing-original draft. **Houshyar Noshad**: Conceptualization, Project administration, and Supervision. **Ould el Moctar**: Conceptualization, Methodology, Project administration, and Supervision.

## Declaration of Interests

The author declares that he has no known competing financial interests or personal relationships that could have appeared to influence the work reported in this paper.


## Funding

This research did not receive any specific grant from funding agencies in the public, commercial, or not-for-profit sectors.

## Acknowledgments

The authors gratefully acknowledge Polish high-performance computing infrastructure PLGrid (HPC Centers: WCSS, ACK Cyfronet AGH) for providing computer facilities and support within computational grant no. PLG/2025/018166.

**References**

[1] V. Blay, R.E. Galian, L.M. Muresan, D. Pankratov, P. Pinyou, G. Zampardi, Research Frontiers in Energy-Related Materials and Applications for 2020–2030, Advanced Sustainable Systems 4 (2020) 1900145. https://doi.org/10.1002/adsu.201900145.

[2] T. Kim, W. Song, D.-Y. Son, L.K. Ono, Y. Qi, Lithium-ion batteries: outlook on present, future, and hybridized technologies, J. Mater. Chem. A 7 (2019) 2942–2964. https://doi.org/10.1039/C8TA10513H.

[3] Y. Rao, J. Yang, S. Chu, S. Guo, H. Zhou, Solid-state Li–air batteries: Fundamentals, challenges, and strategies, SmartMat 4 (2023) e1205. https://doi.org/10.1002/smm2.1205.

[4] S. Song, F.U. Rehman, D.-R. Chang, S.P. Jung, N.R. Singha, M. Chang, Advancing the lithium-air battery performance with hydroxy-TEMPO as a redox mediator: A route to improved efficiency and cycle stability, Journal of Energy Storage 127 (2025) 117068. https://doi.org/10.1016/j.est.2025.117068.

[5] Y.I. Lee, D.G. Kang, Y. Joo, H. Kwon, Y.S. Cho, K.H. Ryu, M.S. Kim, Mechanical balance of plant design of lithium-air batteries for electric vehicles, Journal of Energy Storage 70 (2023) 107969. https://doi.org/10.1016/j.est.2023.107969.

[6] J.P. Pender, G. Jha, D.H. Youn, J.M. Ziegler, I. Andoni, E.J. Choi, A. Heller, B.S. Dunn, P.S. Weiss, R.M. Penner, C.B. Mullins, Electrode Degradation in Lithium-Ion Batteries, ACS Nano 14 (2020) 1243–1295. https://doi.org/10.1021/acsnano.9b04365.

[7] S. Rezaee, H. Araghi, H. Noshad, Z. Zabihi, Physical characteristics of fluorine-doped lithium oxide as advanced material for solid-electrolyte-interphase applications of lithium–air batteries, Eur. Phys. J. Plus 137 (2022) 1194. https://doi.org/10.1140/epjp/s13360-022-03345-8.

[8] W. Li, Y. Wang, N. Xu, Y. Li, High-entropy spinel oxides as efficient ORR catalysts towards enhanced kinetics for zinc-air batteries, Journal of Energy Storage 123 (2025) 116784. https://doi.org/10.1016/j.est.2025.116784.

[9] C. Wang, Z. Xie, Z. Zhou, Lithium-air batteries: Challenges coexist with opportunities, APL Materials 7 (2019) 040701. https://doi.org/10.1063/1.5091444.

[10] J. Xiao, D. Wang, W. Xu, D. Wang, R.E. Williford, J. Liu, J.-G. Zhang, Optimization of Air Electrode for Li/Air Batteries, J. Electrochem. Soc. 157 (2010) A487. https://doi.org/10.1149/1.3314375.

[11] M. Yu, T. Zhang, J. Li, H. Sun, Performance and catalytic mechanism of CNTs/Ti3C2Tx MXene composite cathode for air-breathing hybrid lithium-air batteries, Journal of Energy Storage 101 (2024) 113725. https://doi.org/10.1016/j.est.2024.113725.

[12] Q. Pan, L. Fu, Z. Wang, Z. Zhong, J. Zhao, Research progress on MXenes-based electrocatalysts with high oxygen activity for air cathodes in metal-air batteries, Journal of Energy Storage 111 (2025) 115388. https://doi.org/10.1016/j.est.2025.115388.

[13] Z. Hu, G. Yang, X. Li, P. Kong, M. Zhen, B. Shen, Recycling and application of cathode materials for lithium-ion batteries, Journal of Energy Storage 134 (2025) 118099. https://doi.org/10.1016/j.est.2025.118099.

[14] Critical Challenges in Rechargeable Aprotic Li–O2 Batteries - Feng - 2016 - Advanced Energy Materials - Wiley Online Library, (n.d.). https://advanced.onlinelibrary.wiley.com/doi/full/10.1002/aenm.201502303 (accessed May 27, 2025).

[15] D. Geng, N. Ding, T.S.A. Hor, S.W. Chien, Z. Liu, D. Wuu, X. Sun, Y. Zong, From Lithium-Oxygen to Lithium-Air Batteries: Challenges and Opportunities, Advanced Energy Materials 6 (2016) 1502164. https://doi.org/10.1002/aenm.201502164.

[16] Z. Tong, Z. Li, L. Tan, Y. Li, L. Wang, Y. Shang, J. Bi, H. Jiang, S. Lei, W. Zhu, L. Zhang, Recent advances in synthesis and modification strategies for lithium-ion battery ternary cathodes, Journal of Energy Storage 98 (2024) 113085. https://doi.org/10.1016/j.est.2024.113085.

[17] A. Behravan, M. Aghaie-Khafri, A novel approach for facile synthesis of cost-optimal catalyst for high-performance lithium-air battery, Journal of Energy Storage 86 (2024) 111231. https://doi.org/10.1016/j.est.2024.111231.

[18] H. Xu, L. Jin, X. Qian, B. Li, Design of carbon-coated MnCo bimetallic oxide as an efficient oxygen reduction catalyst and its application in zinc-air batteries, Journal of Energy Storage 125 (2025) 117018. https://doi.org/10.1016/j.est.2025.117018.

[19] H. Kang, Y. Xiao, Q. Feng, B. Su, Z. Lei, Nitrogen-doped carbon self-supported NiFeCo phosphide bifunctional electrocatalysts for rechargeable zinc-air batteries, Journal of Energy Storage 111 (2025) 115444. https://doi.org/10.1016/j.est.2025.115444.

[20] J.-J. Xu, Z.-L. Wang, D. Xu, F.-Z. Meng, X.-B. Zhang, 3D ordered macroporous LaFeO3 as efficient electrocatalyst for Li–O2 batteries with enhanced rate capability and cyclic performance, Energy Environ. Sci. 7 (2014) 2213–2219. https://doi.org/10.1039/C3EE42934B.

[21] Z. Ma, X. Yuan, L. Li, Z.-F. Ma, D.P. Wilkinson, L. Zhang, J. Zhang, A review of cathode materials and structures for rechargeable lithium–air batteries, Energy Environ. Sci. 8 (2015) 2144–2198. https://doi.org/10.1039/C5EE00838G.

[22] D.B. Meadowcroft, Low-cost Oxygen Electrode Material, Nature 226 (1970) 847–848. https://doi.org/10.1038/226847a0.

[23] Y. Matsumoto, E. Sato, Electrocatalytic properties of transition metal oxides for oxygen evolution reaction, Materials Chemistry and Physics 14 (1986) 397–426. https://doi.org/10.1016/0254-0584(86)90045-3.

[24] J.O. Bockris, T. Otagawa, The Electrocatalysis of Oxygen Evolution on Perovskites, J. Electrochem. Soc. 131 (1984) 290. https://doi.org/10.1149/1.2115565.

[25] T. Hyodo, M. Hayashi, N. Miura, N. Yamazoe, Catalytic Activities of Rare-Earth Manganites for Cathodic Reduction of Oxygen in Alkaline Solution, J. Electrochem. Soc. 143 (1996) L266. https://doi.org/10.1149/1.1837229.

[26] W.-J. Yin, B. Weng, J. Ge, Q. Sun, Z. Li, Y. Yan, Oxide perovskites, double perovskites and derivatives for electrocatalysis, photocatalysis, and photovoltaics, Energy Environ. Sci. 12 (2019) 442–462. https://doi.org/10.1039/C8EE01574K.

[27] Z. Ma, X. Yuan, L. Li, Z.-F. Ma, The double perovskite oxide Sr2CrMoO6−δ as an efficient electrocatalyst for rechargeable lithium air batteries, Chem. Commun. 50 (2014) 14855–14858. https://doi.org/10.1039/C4CC06113F.

[28] L. Chen, J. Ding, X. Zhu, A review on research progress of double perovskite oxides for oxygen evolution reaction electrocatalysts and supercapacitors, RSC Applied Interfaces 2 (2025) 320–351. https://doi.org/10.1039/D4LF00395K.

[29] B. Hua, Y.-F. Sun, M. Li, N. Yan, J. Chen, Y.-Q. Zhang, Y. Zeng, B. Shalchi Amirkhiz, J.-L. Luo, Stabilizing Double Perovskite for Effective Bifunctional Oxygen Electrocatalysis in Alkaline Conditions, Chem. Mater. 29 (2017) 6228–6237. https://doi.org/10.1021/acs.chemmater.7b01114.

[30] B. Zhao, L. Zhang, D. Zhen, S. Yoo, Y. Ding, D. Chen, Y. Chen, Q. Zhang, B. Doyle, X. Xiong, M. Liu, A tailored double perovskite nanofiber catalyst enables ultrafast oxygen evolution, Nat Commun 8 (2017) 14586. https://doi.org/10.1038/ncomms14586.

[31] C. Chen, D. Chen, F. Ciucci, A molecular dynamics study of oxygen ion diffusion in A-site ordered perovskite PrBaCo2O5.5: data mining the oxygen trajectories, Phys. Chem. Chem. Phys. 17 (2015) 7831–7837. https://doi.org/10.1039/C4CP05847J.

[32] I. Kim, M. Choi, First-Principles Study of Anisotropic Oxygen Diffusion in PrBaCo2O5.5, ACS Omega 4 (2019) 10960–10964. https://doi.org/10.1021/acsomega.9b01049.

[33] U. Anjum, M. Agarwal, T.S. Khan, M.A. Haider, Mechanistic Elucidation of Surface Cation Segregation in Double Perovskite PrBaCo2O5+δ Material using MD and DFT Simulations for Solid Oxide Fuel Cells, Ionics 26 (2020) 1307–1314. https://doi.org/10.1007/s11581-019-03318-5.

[34] U. Anjum, S. Vashishtha, M. Agarwal, P. Tiwari, N. Sinha, A. Agrawal, S. Basu, M.A. Haider, Oxygen anion diffusion in double perovskite GdBaCo2O5+δ and LnBa0.5Sr0.5Co2−xFexO5+δ (Ln = Gd, Pr, Nd) electrodes, International Journal of Hydrogen Energy 41 (2016) 7631–7640. https://doi.org/10.1016/j.ijhydene.2016.02.090.

[35] U. Anjum, S. Vashishtha, N. Sinha, M.A. Haider, Role of oxygen anion diffusion in improved electrochemical performance of layered perovskite LnBa1 − ySryCo2 − xFexO5 + δ (Ln = Pr, Nd, Gd) electrodes, Solid State Ionics 280 (2015) 24–29. https://doi.org/10.1016/j.ssi.2015.08.002.

[36] M.Z. Galin, A.K. Ivanov-Schitz, G.N. Mazo, Molecular Dynamics Simulation of Structural and Transport Properties of Solid Solutions of Double Perovskites Based on PrBaCo2O5.5, Crystallogr. Rep. 65 (2020) 289–296. https://doi.org/10.1134/S106377452002008X.

[37] S.R. Choi, I.-S. So, S.W. Lee, J. Yoo, Y.-S. Seo, H.-S. Cho, J.-Y. Park, 3D architecture double perovskite NdBa0.5Sr0.5Co1.5Fe0.5O5+δ embedded hollow-net Co3O4 bifunctional electrocatalysts coupled with N-doped CNT and reduced graphene oxide for oxygen electrode reactions, Journal of Alloys and Compounds 823 (2020) 153782. https://doi.org/10.1016/j.jallcom.2020.153782.

[38] N.-I. Kim, S.-H. Cho, S.H. Park, Y.J. Lee, R.A. Afzal, J. Yoo, Y.-S. Seo, Y.J. Lee, J.-Y. Park, B-site doping effects of NdBa0.75Ca0.25Co2O5+δ double perovskite catalysts for oxygen evolution and reduction reactions, J. Mater. Chem. A 6 (2018) 17807–17818. https://doi.org/10.1039/C8TA06236F.

[39] A. Maignan, C. Martin, D. Pelloquin, N. Nguyen, B. Raveau, Structural and Magnetic Studies of Ordered Oxygen-Deficient Perovskites*Ln*BaCo2O5+δ, Closely Related to the “112” Structure, Journal of Solid State Chemistry 142 (1999) 247–260. https://doi.org/10.1006/jssc.1998.7934.

[40] S. Streule, A. Podlesnyak, J. Mesot, M. Medarde, K. Conder, E. Pomjakushina, E. Mitberg, V. Kozhevnikov, Effect of oxygen ordering on the structural and magnetic properties of the layered perovskites PrBaCo2O5+δ, J. Phys.: Condens. Matter 17 (2005) 3317. https://doi.org/10.1088/0953-8984/17/21/024.

[41] I.D. Seymour, A. Chroneos, J.A. Kilner, R.W. Grimes, Defect processes in orthorhombic LnBaCo2O5.5 double perovskites, Phys. Chem. Chem. Phys. 13 (2011) 15305–15310. https://doi.org/10.1039/C1CP21471C.

[42] I.D. Seymour, A. Tarancón, A. Chroneos, D. Parfitt, J.A. Kilner, R.W. Grimes, Anisotropic oxygen diffusion in PrBaCo2O5.5 double perovskites, Solid State Ionics 216 (2012) 41–43. https://doi.org/10.1016/j.ssi.2011.09.002.

[43] A.I. Ivanov, V.A. Kolotygin, E.V. Tsipis, S.I. Bredikhin, V.V. Kharton, Electrical Conductivity, Thermal Expansion and Electrochemical Properties of Perovskites PrBaFe2–xNixO5 + δ, Russ J Electrochem 54 (2018) 533–540. https://doi.org/10.1134/S102319351806006X.

[44] A. Klyndyuk, ChemInform Abstract: Layered Perovskite-Like Oxides 0112 Type. Structure, Properties, and Possible Applications, ChemInform 42 (2011). https://doi.org/10.1002/chin.201113227.

[45] Z. Xie, H. Zhao, T. Chen, X. Zhou, Z. Du, Synthesis and electrical properties of Al-doped Sr2MgMoO6-δ as an anode material for solid oxide fuel cells, International Journal of Hydrogen Energy 36 (2011) 7257–7264. https://doi.org/10.1016/j.ijhydene.2011.03.075.

[46] Y. Bu, O. Gwon, G. Nam, H. Jang, S. Kim, Q. Zhong, J. Cho, G. Kim, A Highly Efficient and Robust Cation Ordered Perovskite Oxide as a Bifunctional Catalyst for Rechargeable Zinc-Air Batteries, ACS Nano 11 (2017) 11594–11601. https://doi.org/10.1021/acsnano.7b06595.

[47] X. Pan, X. Zhu, J. Qin, Y. Wu, W. Wan, T. Chen, Y. Wang, Z. Man, Z. Lü, Performance evaluation of carbon/PrBaCo2O5+δ composite electrodes for Li–O2 batteries, International Journal of Hydrogen Energy 46 (2021) 8539–8548. https://doi.org/10.1016/j.ijhydene.2020.12.046.

[48] S. Streule, A. Podlesnyak, D. Sheptyakov, E. Pomjakushina, M. Stingaciu, K. Conder, M. Medarde, M.V. Patrakeev, I.A. Leonidov, V.L. Kozhevnikov, J. Mesot, High-temperature order-disorder transition and polaronic conductivity in ${\mathrm{PrBaCo}}_{2}{\mathrm{O}}_{5.48}$, Phys. Rev. B 73 (2006) 094203. https://doi.org/10.1103/PhysRevB.73.094203.

[49] S. Streule, A. Podlesnyak, E. Pomjakushina, K. Conder, D. Sheptyakov, M. Medarde, J. Mesot, Oxygen order–disorder phase transition in PrBaCo2O5.48 at high temperature, Physica B: Condensed Matter 378–380 (2006) 539–540. https://doi.org/10.1016/j.physb.2006.01.244.

[50] J. Hermet, G. Geneste, G. Dezanneau, Molecular dynamics simulations of oxygen diffusion in GdBaCo2O5.5, Applied Physics Letters 97 (2010) 174102. https://doi.org/10.1063/1.3504250.

[51] X. Liu, M. Zhu, Z. Chen, B. Fang, J. Ding, X. Zhao, H. Xu, H. Luo, Structure and electrical properties of Li-doped BaTiO3–CaTiO3–BaZrO3 lead-free ceramics prepared by citrate method, Journal of Alloys and Compounds 613 (2014) 219–225. https://doi.org/10.1016/j.jallcom.2014.06.046.

[52] S. Plimpton, Fast Parallel Algorithms for Short-Range Molecular Dynamics, Journal of Computational Physics 117 (1995) 1–19. https://doi.org/10.1006/jcph.1995.1039.

[53] W. Humphrey, A. Dalke, K. Schulten, VMD: Visual molecular dynamics, Journal of Molecular Graphics 14 (1996) 33–38. https://doi.org/10.1016/0263-7855(96)00018-5.

[54] A. Stukowski, Visualization and analysis of atomistic simulation data with OVITO–the Open Visualization Tool, Modelling Simul. Mater. Sci. Eng. 18 (2009) 015012. https://doi.org/10.1088/0965-0393/18/1/015012.

[55] W.C. Swope, H.C. Andersen, P.H. Berens, K.R. Wilson, A computer simulation method for the calculation of equilibrium constants for the formation of physical clusters of molecules: Application to small water clusters, The Journal of Chemical Physics 76 (1982) 637–649. https://doi.org/10.1063/1.442716.

[56] S. Rezaee, H. Araghi, H. Noshad, Z. Zabihi, Physical characteristics of nickel thin-films and nickel thin-film foams as Li-air batteries anode and cathode current collectors, Journal of Molecular Liquids 383 (2023) 122171. https://doi.org/10.1016/j.molliq.2023.122171.

[57] G.V. Lewis, C.R.A. Catlow, Defect studies of doped and undoped barium titanate using computer simulation techniques, Journal of Physics and Chemistry of Solids 47 (1986) 89–97. https://doi.org/10.1016/0022-3697(86)90182-4.

[58] C.A.J. Fisher, M. Yoshiya, Y. Iwamoto, J. Ishii, M. Asanuma, K. Yabuta, Oxide ion diffusion in perovskite-structured Ba1−xSrxCo1−yFeyO2.5: A molecular dynamics study, Solid State Ionics 177 (2007) 3425–3431. https://doi.org/10.1016/j.ssi.2006.03.060.

[59] G.V. Lewis, C.R.A. Catlow, Potential models for ionic oxides, J. Phys. C: Solid State Phys. 18 (1985) 1149. https://doi.org/10.1088/0022-3719/18/6/010.

[60] W. Körner, C. Elsässer, Density-functional theory study of stability and subgap states of crystalline and amorphous Zn–Sn–O, Thin Solid Films 555 (2014) 81–86. https://doi.org/10.1016/j.tsf.2013.05.146.

[61] E.-L. Rautama, M. Karppinen, *R*-site varied series of *R*BaCo2O5.5 (*R*2Ba2Co4O11) compounds with precisely controlled oxygen content, Journal of Solid State Chemistry 183 (2010) 1102–1107. https://doi.org/10.1016/j.jssc.2010.03.011.

[62] F. Hesse, I. da Silva, J.-W.G. Bos, Insights into Oxygen Migration in LaBaCo2O6−δ Perovskites from In Situ Neutron Powder Diffraction and Bond Valence Site Energy Calculations, Chem. Mater. 34 (2022) 1191–1202. https://doi.org/10.1021/acs.chemmater.1c03726.

[63] G. Kim, S. Wang, A.J. Jacobson, L. Reimus, P. Brodersen, C.A. Mims, Rapid oxygen ion diffusion and surface exchange kinetics in PrBaCo2O5+x with a perovskite related structure and ordered A cations, J. Mater. Chem. 17 (2007) 2500–2505. https://doi.org/10.1039/B618345J.

[64] Z. Wang, Y. Sun, H. Kong, C. Xia-Bauer, An in-depth review of key technologies and pathways to carbon neutrality: classification and assessment of decarbonization technologies, Carb Neutrality 4 (2025) 15. https://doi.org/10.1007/s43979-025-00129-8.

[65] M. deCastro, S. Salvador, M. Gómez-Gesteira, X. Costoya, D. Carvalho, F.J. Sanz-Larruga, L. Gimeno, Europe, China and the United States: Three different approaches to the development of offshore wind energy, Renewable and Sustainable Energy Reviews 109 (2019) 55–70. https://doi.org/10.1016/j.rser.2019.04.025.

[66] I. Perissi, A. Jones, Investigating European Union Decarbonization Strategies: Evaluating the Pathway to Carbon Neutrality by 2050, Sustainability 14 (2022) 4728. https://doi.org/10.3390/su14084728.

[67] A. Sahu, N. Yadav, K. Sudhakar, Floating photovoltaic power plant: A review, Renewable and Sustainable Energy Reviews 66 (2016) 815–824. https://doi.org/10.1016/j.rser.2016.08.051.

[68] L. Li, Y. Gao, Z. Yuan, S. Day, Z. Hu, Dynamic response and power production of a floating integrated wind, wave and tidal energy system, Renewable Energy 116 (2018) 412–422. https://doi.org/10.1016/j.renene.2017.09.080.

[69] H. Khaloie, A. Anvari-Moghaddam, J. Contreras, J.-F. Toubeau, P. Siano, F. Vallée, Offering and bidding for a wind producer paired with battery and CAES units considering battery degradation, International Journal of Electrical Power & Energy Systems 136 (2022) 107685. https://doi.org/10.1016/j.ijepes.2021.107685.

[70] J. Bai, T. Ding, W. Jia, C. Mu, P. Siano, M. Shahidehpour, Battery Charging and Swapping System Involved in Demand Response for Joint Power and Transportation Networks, IEEE Transactions on Intelligent Transportation Systems 25 (2024) 6836–6847. https://doi.org/10.1109/TITS.2023.3346403.

[71] G.L. Kyriakopoulos, G. Arabatzis, Electrical energy storage systems in electricity generation: Energy policies, innovative technologies, and regulatory regimes, Renewable and Sustainable Energy Reviews 56 (2016) 1044–1067. https://doi.org/10.1016/j.rser.2015.12.046.

[72] X. Zhang, X.-G. Wang, Z. Xie, Z. Zhou, Recent progress in rechargeable alkali metal–air batteries, Green Energy & Environment 1 (2016) 4–17. https://doi.org/10.1016/j.gee.2016.04.004.

[73] P.G. Bruce, S.A. Freunberger, L.J. Hardwick, J.-M. Tarascon, Li–O2 and Li–S batteries with high energy storage, Nature Mater 11 (2012) 19–29. https://doi.org/10.1038/nmat3191.

[74] M. Abdirakhimov, M.H. Al-Rashed, J. Wójcik, Recent Attempts on the Removal of H2S from Various Gas Mixtures Using Zeolites and Waste-Based Adsorbents, Energies 15 (2022) 5391. https://doi.org/10.3390/en15155391.

[75] J.-H. Kang, J. Lee, J.-W. Jung, J. Park, T. Jang, H.-S. Kim, J.-S. Nam, H. Lim, K.R. Yoon, W.-H. Ryu, I.-D. Kim, H.R. Byon, Lithium–Air Batteries: Air-Breathing Challenges and Perspective, ACS Nano 14 (2020) 14549–14578. https://doi.org/10.1021/acsnano.0c07907.

[76] V.S. Saji, Nanocarbons-Based Trifunctional Electrocatalysts for Overall Water Splitting and Metal-Air Batteries: Metal-Free and Hybrid Electrocatalysts, Chemistry – An Asian Journal 19 (2024) e202400712. https://doi.org/10.1002/asia.202400712.

[77] W. Shang, H. Wang, W. Yu, Y. He, Y. Ma, R. Li, Z. Wu, P. Tan, A zinc-air battery capable of working in anaerobic conditions and fast environmental energy harvesting, Cell Reports Physical Science 3 (2022) 100904. https://doi.org/10.1016/j.xcrp.2022.100904.

[78] F. Meng, P. Chen, S. Li, N. Cao, S. Cheng, X. Wei, J. Di, J. Liu, Fish-Gill-Inspired Underwater Self-Breathing Zinc–Air Batteries, ACS Appl. Energy Mater. 7 (2024) 9442–9450. https://doi.org/10.1021/acsaem.4c01992.

[79] B. Mortazavi, T. Rabczuk, X. Zhuang, Exploring the structural stability, thermal and mechanical properties of nanoporous carbon nitride nanosheets using a transferrable machine learning interatomic potential, Mach. Learn. Comput. Sci. Eng 1 (2024) 5. https://doi.org/10.1007/s44379-024-00008-6.

[80] B. Mortazavi, M. Shahrokhi, F. Shojaei, T. Rabczuk, X. Zhuang, A.V. Shapeev, A first-principles and machine-learning investigation on the electronic, photocatalytic, mechanical and heat conduction properties of nanoporous C5N monolayers, Nanoscale 14 (2022) 4324–4333. https://doi.org/10.1039/D1NR06449E.